Numerical Analysis of Energy Expenditure for Coflow Wall Jet Separation Control

Kewei Xu,* Yan Ren,† and Gecheng Zha‡
University of Miami, Coral Gables, Florida 33124

https://doi.org/10.2514/1.J061015

This paper numerically investigates the energy expenditure of the coflow wall jet for separation control by analyzing the widely studied NASA hump with two-dimensional unsteady Reynolds averaged Navier–Stokes equations. The coflow wall jet is shown to be effective in both adverse and favorable pressure gradients but is more efficient in adverse pressure gradients due to lower velocity, lower entropy increase, and more enhanced mixing. An energy-efficient way to devise a coflow wall jet flow control is twofold: 1) place the injection near the separation onset point at a slightly downstream location, and 2) place the suction slot further downstream with sufficiently long distance in adverse pressure gradient region for a thorough mixing and energy transfer. The vanishing of the counterclockwise wall jet vorticity appears to indicate a sufficient mixing distance. In that case, the injection plays the dominant role. The suction makes a small contribution with a weak coupling effect but primarily serves as the flow source for the mass conservation of the zero-net-mass-flux flow control, which is essential to be energy efficient. The coflow wall jet is also compared with the injection-only and suction-only flow controls, which are effective if the slots are placed at the desirable position slightly downstream of the separation onset point. But if they are not placed near the separation onset locations, the coflow wall jet is much more efficient and effective than the injection-only or suction-only flow controls due to the coupling effect between the injection and suction.

Nomenclature

AFC	=	active flow control
AoA	=	angle of attack
APG	=	adverse pressure gradient
BC	=	boundary condition
$CFWJ$	=	coflow wall jet
C_E	=	energy coefficient, $\dot{m}_j U_j^2/(0.5 q_{\text{ref}} U_{\text{ref}} S)$
C_L	=	lift coefficient
C_p	=	pressure coefficient
C_μ	=	jet momentum coefficient, $\dot{m}_j U_j/(q_{\text{ref}} S)$
c	=	hump chord length
$FASIP$	=	flow–acoustics–structure interaction package
FPG	=	favorable pressure gradient
H_t	=	total enthalpy
h	=	slot height
LE	=	leading edge
Ma	=	Mach number
$\dot{m}$	=	mass flow rate, ρUA
$\bar{\dot{m}}$	=	normalized mass flow rate, $\dot{m}/\rho_{\text{ref}} U_{\text{ref}} A_{\text{ref}}$
P	=	coflow wall jet pumping power
PR	=	power required
P_c	=	power coefficient
P_t	=	total pressure
q_{ref}	=	freestream dynamic pressure, $0.5\rho_{\text{ref}} U_{\text{ref}}^2$
Re	=	Reynolds number
T_t	=	total temperature
$URANS$	=	unsteady Reynolds-averaged Navier–Stokes
U_j	=	injection jet velocity
U_{ref}	=	reference velocity at inlet
U_∞	=	freestream velocity away from wall
VP	=	velocity profile
$ZNMF$	=	zero-net mass flux
α	=	angle of attack
β	=	sideslip angle
Γ	=	total pressure ratio
γ	=	air specific heat ratio
δ^*	=	displacement thickness
η	=	coflow wall jet pumping system efficiency
θ	=	momentum thickness
ρ_{ref}	=	reference density
τ	=	shear stress

Subscripts

c	=	corrected
j	=	jet
ref	=	reference parameters at hump inlet
t	=	total value
∞	=	freestream flow away from wall

Received 20 June 2021; revision received 27 October 2021; accepted for publication 14 November 2021; published online 10 January 2022.

*Ph.D. Candidate, Department of Mechanical and Aerospace Engineering.
†Post-Doctoral Researcher, Department of Mechanical and Aerospace Engineering.
‡Professor, Department of Mechanical and Aerospace Engineering; gzha@miami.edu. Associate Fellow AIAA.

I. Introduction

ACTIVE flow control (AFC) has the potential to break through conventional fluid mechanics limitations and provides significant performance improvement to fluid systems [1]. AFC is to transfer external energy to the controlled flow in order to improve the performance of the flow system. Prandtl's rotating cylinder experiment in 1934 was one of the earliest AFC studies to transfer mechanical energy to flow via the surface shear stress of a rotating cylinder [2]. However, systematic studies of AFC have only occurred recently due to more and more challenging applications of flow systems.

For all AFC systems, there are three measures of merit (MoM): 1) effectiveness, 2) power required (PR), and 3) power conversion efficiency (PCE). Effectiveness quantifies the performance enhancement, for example, removal of flow separation, drag reduction, lift increase, stall prevention, noise mitigation, and so on. Power required quantifies the AFC power needed to achieve the targeted effectiveness. Power conversion efficiency quantifies the efficiency to convert the external power (e.g., mechanical, electric, and chemical) to the power required by the controlled flow. It determines how much total power will be consumed by the actual flow control system.

For an AFC to benefit industry realistic applications, all three MOM matter. The ultimate criterion for an AFC is that the system efficiency gain should be greater than the AFC energy expenditure. However, the current AFCs do not always have clear quantification of

all the MOM, in particular for the PR and PCE, partially because they may not always be easy to measure. For a zero-net-mass-flux (ZNMF) flow control, it is more straightforward to measure the PR and PCE because it is a closed system. For a non-ZNMF flow control such as the one using injection only, namely, an open system, the PR is difficult to measure because it depends on the path that the mass flow source is supplied. The PCE measurement could be even more difficult because it also depends on the actuators used and their integration with the system (e.g., aircraft). Similarly, for the flow control with suction only, the PR and PCE depend on the path that the flow is discharged to the sink. In other words, the PR and PCE of the non-ZNMF flow control are path dependent. A long path, in general, will suffer from a high-energy loss, in particular, if the path requires a flow turning perpendicular to the controlled flow plane.

Synthetic jets [3–8] generated by the periodic motion of a piston or diagram and plasma jets based on plasma discharge [9–13] are zero-net-mass-flux flow controls, which require no external flow source. However, both the synthetic and plasma jets, in general, provide low input momentum due to low-energy conversion efficiency from electric to fluid power, typically $3 \sim 10\%$ [14–16] for synthetic jets and less than 1% for plasma actuators [17]. The control effectiveness of synthetic and plasma jets is thus limited for high-momentum flows.

The flow control methods using fluidic actuators generally can provide high momentum with a high control authority. An example is the widely used circulation control (CC) relying on jet injection and Coanda effect [18–21]. A CC airfoil is effective to enhance the lift coefficient. However, CC airfoil is an injection-only flow control method. The PR is path dependent, and a systematic study of PR for CC airfoil is not well documented in the published literature.

Recently, a fluidic-actuator-based ZNMF coflow wall jet (CFWJ) AFC achieves airfoil performance enhancement with ultrahigh lift coefficient and high cruise efficiency at low-energy expenditure [22–29]. As sketched in Fig. 1, a CFWJ airfoil draws a small amount of mass flow into the airfoil near the trailing edge, pressurizes and energizes it using a microcompressor embedded inside the airfoil, and then tangentially injects the same mass flow near the leading edge in the main flow direction.

The coflow wall jet has a tangential injection to the wall surface with a streamwise suction downstream. Hence, the CFWJ is categorized as a wall jet [30–36]. In this paper, the term *coflow wall jet* means the same as *coflow jet* (CFJ), which is used in other previous publications [22–29,37–40]. CFWJ and CFJ are interchangeable. CFWJ AFC always comes in pair with an injection and suction to form a closed mass conservation system on the flow control plane. In other words, CFWJ is a ZNMF flow control that combines the features of a wall jet and boundary layer suction. Xu et al. [38] investigate the CFWJ separation control mechanism. This paper is focused on the CFWJ energy expenditure.

As shown in Fig. 1, the microcompressor actuator withdraws the low-energy flow downstream caused by total pressure loss, energizes the flow, and injects the high-energy flow upstream to energize the boundary layer so that it can overcome severe adverse pressure gradients (APGs) [25,26,41]. Such energy transfer direction determines that the suction be located downstream and the injection be located upstream. The jet mass flow transportation and energization process through the microcompressor actuator have the opposite flow direction to the main flow as shown in Fig. 1. The advantage to place the injection upstream is that it requires a relatively low power to eject the flow when the external main flow pressure is low. Similarly, placing the suction downstream with the high external main flow pressure due to APG makes the suction easier. Such an injection and suction distribution is desirable to minimize the energy expenditure. Since this process is local with a short path, it can achieve a high efficiency due to a low total pressure loss, for example, 1–2% [42] by designing the injection and suction ducts with smooth turning and no flow separation.

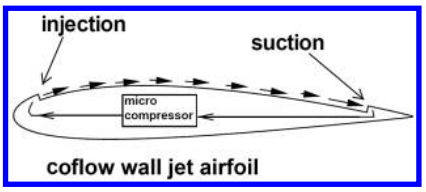

Fig. 1 Schematics of the CFWJ airfoil.

Because the CFWJ is a zero-net-mass-flux flow control method, the power required is well defined by the total enthalpy rise from the suction duct outlet (compressor inlet) to the injection duct inlet (compressor outlet) [24]. The total enthalpy rise can be achieved by the embedded microcompressors or other pumping systems. The power required PR at the CFWJ can be expressed as

$$PR = \dot{m} H_{t2} (\Gamma^{\gamma-1/\gamma} - 1) \tag{1}$$

where $\dot{m}$ is the CFWJ mass flow rate, H_{t2} is the total enthalpy at the suction slot, Γ is the total pressure ratio between the injection and suction, and γ is the ratio of specific heat and takes the value of 1.4 for ideal gas.

The power coefficient is defined as

$$P_c = \frac{PR}{(1/2)\rho_{\text{ref}} U_{\text{ref}}^3 A_{\text{ref}}} \tag{2}$$

where ρ_{ref} and U_{ref} denote the reference density and velocity at the inlet and A_{ref} is the reference area defined as the product of chord length and hump span in this study.

Equation (1) indicates that the power required by the CFWJ is determined linearly by the mass flow rate and exponentially by the total pressure ratio. This provides a principle to reduce CFWJ power consumption; it is desirable to have a high mass flow rate and low total pressure ratio as the latter increases much faster than the former. This relationship in fact applies to all active flow controls based on fluidic actuators. To be general and focus on the AFC performance, only the power required defined in Eq. (1) is studied in this paper.

The actual total power consumed by CFWJ is

$$P_{\text{total}} = PR/\eta \tag{3}$$

where η is the PCE of the microcompressor system. The typical microcompressors used for small general aviation aircraft have a diameter of 5–7 cm, which allows a fairly high power conversion efficiency up to 85% [26,42–44]. If the applications are for large aircraft, the size of the compressors will be also larger, and the efficiency could be even higher.

A parameter widely used to describe the jet strength is the jet momentum coefficient C_μ defined as

$$C_\mu = \frac{\dot{m} U_j}{(1/2)\rho_{\text{ref}} U_{\text{ref}}^2 A_{\text{ref}}} \tag{4}$$

where U_j is the mass-averaged injection velocity. As indicated by Zha et al. [27], C_μ only represents a part of the injection thrust. The total reactionary force created by an AFC with fluidic actuator includes the injection thrust and the ram drag created by the suction [27]. Because a flow control with injection only is not straightforward to calculate the total power by Eq. (1) without the information of the flow path (i.e., Γ), C_μ sometimes was used to represent the added equivalent drag or power coefficient caused by the injection [45], such as $(C_D)_{\text{corrected}} = C_D + C_\mu$. However, C_μ does not behave in the same way as the power coefficient quantitatively and qualitatively. The proper way to convert the AFC power required to the added equivalent drag is $(C_D)_{\text{corrected}} = C_D + P_c$, where P_c is defined by Eq. (2) [24–26]. A high C_μ could have a lower power consumption than a smaller C_μ if the high C_μ is obtained by a high mass flow rate and low jet velocity, which may result in a significantly lower total pressure ratio [41,46,47].

For a typical CFWJ airfoil, the mixing process between the wall jet and main flow starts at the near lowest pressure location of the airfoil behind the leading edge and ends near the highest pressure location upstream of the trailing edge as shown in Fig. 2a. The CFWJ covers

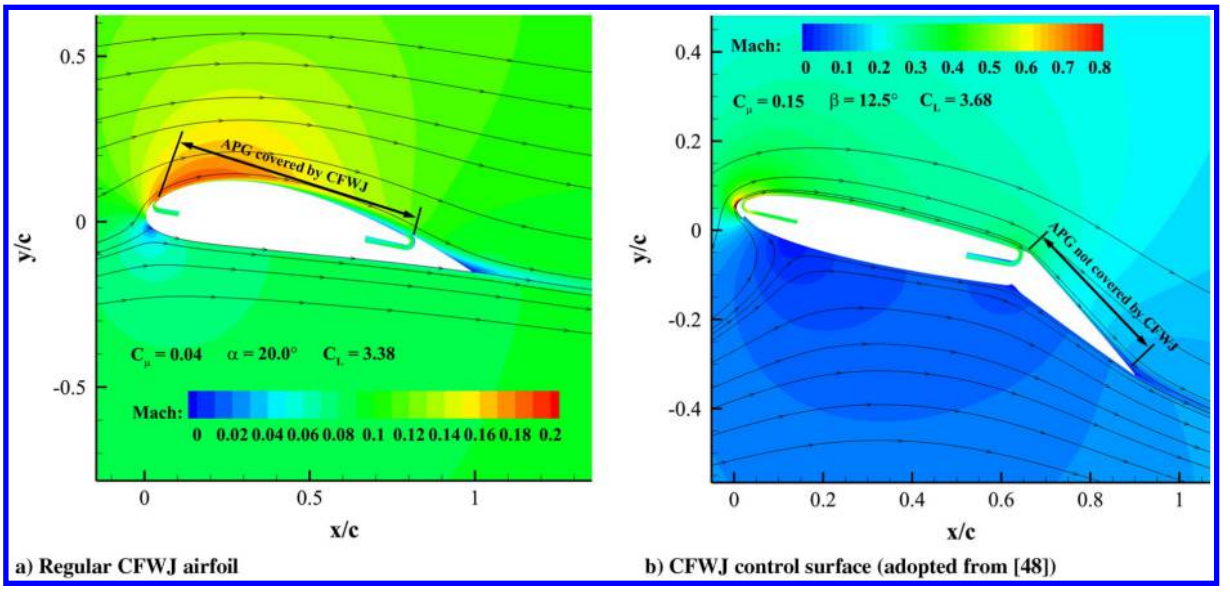

Fig. 2 Mach number contours of CFWJ applications.

the area of the APG. For a CFWJ flight control surface application [29,48,49] as shown in Fig. 2b, the coflow wall jet is not extended to the deflected flap area due to structure consideration. The severe APG area of a control surface is mostly in the flap area, which is uncovered by the coflow wall jet. However, a significant improvement of control surface lift coefficient C_L is still achieved with fairly high-energy efficiency [29,48,49].

The mentioned phenomena trigger the following questions. What is the respective role of the injection and suction of CFWJ to minimize its energy expenditure? What is the desirable location to place the CFWJ injection and suction? Is there a coupling effect between the injection and suction? What pressure gradient is more beneficial to CFWJ, the adverse pressure gradient or favorable pressure gradient (FPG)? The purpose of this paper is to answer these questions by investigating the energy expenditure of CFWJ using the widely studied NASA hump for separation control. Understanding the energy expenditure is crucial for practical applications.

The NASA hump [50,51] is often used as a benchmark experiment for various AFC studies, including steady injection [52–54], steady suction [50,52], unsteady injection [55], synthetic jets [7,8], and sweeping jets [54,56,57]. However, most of these studies focus on control effectiveness, whereas the efficiency or energy expenditure is rarely addressed. Borgmann et al. [54] use energy coefficient C_E to measure the power consumption of sweeping jets, which is an injection-only flow control. However, C_E represents the jet kinetic energy, which is similar to the jet momentum coefficient and does not represent the required AFC power determined by the total enthalpy rise. For numerical simulation of ZNMF synthetic jets, the power required to drive the actuator's reciprocating motion is also difficult to evaluate because it is case dependent. Benefiting from the well-defined power required for CFWJ by Eq. (1), this paper systematically investigates the energy expenditure mechanism of the highly effective CFWJ separation control. The results may apply to general active flow controls with tangential injection and streamwise suction.

II. Numerical Approaches

A. Governing Equations

The governing equations for the computational fluid dynamics (CFD) simulation are the unsteady Reynolds-averaged Navier–Stokes equations (URANS) with the one-equation Spalart–Allmaras (SA) turbulence model [58], which are solved in a fully coupled manner using an implicit unfactored Gauss–Seidel line iteration to achieve a high convergence rate [59]. The normalized Navier–Stokes governing equations in generalized coordinates are expressed as

$$\frac{\partial \boldsymbol{Q}}{\partial t} + \frac{\partial \boldsymbol{E}}{\partial \xi} + \frac{\partial \boldsymbol{F}}{\partial \eta} + \frac{\partial \boldsymbol{G}}{\partial \zeta} = \frac{1}{Re}\left[\frac{\partial \boldsymbol{R}}{\partial \xi} + \frac{\partial \boldsymbol{S}}{\partial \eta} + \frac{\partial \boldsymbol{T}}{\partial \zeta}\right] + \boldsymbol{S}_\nu \tag{5}$$

where Re is the Reynolds number. The conservative variable vector $\boldsymbol{Q}$, inviscid flux $\boldsymbol{E}$, and viscous flux vector $\boldsymbol{R}$ are given in the following, and the rest can be expressed following the symmetric rule:

$$\boldsymbol{Q} = \frac{1}{J}\begin{bmatrix} \rho \\ \rho u \\ \rho v \\ \rho w \\ \rho e \\ \rho \hat{\nu} \end{bmatrix}, \qquad \boldsymbol{E} = \frac{1}{J}\begin{bmatrix} \rho U \\ \rho u U + p\xi_x \\ \rho v U + p\xi_y \\ \rho w U + p\xi_z \\ (\rho e + p)U \\ \rho \hat{\nu} U \end{bmatrix},$$

$$\boldsymbol{R} = \frac{1}{J}\begin{bmatrix} 0 \\ \tau_{xi}\xi_i \\ \tau_{yi}\xi_i \\ \tau_{zi}\xi_i \\ (u_j\tau_{ij} - q_i)\xi_i \\ \frac{\rho}{\sigma}(\nu + \hat{\nu})\frac{\partial \hat{\nu}}{\partial x_i}\xi_i \end{bmatrix}, \qquad \boldsymbol{S}_\nu = \begin{bmatrix} 0 \\ 0 \\ 0 \\ 0 \\ 0 \\ S_\nu \end{bmatrix}$$

The $\boldsymbol{S}_\nu$ in Eq. (5) is the source term for the SA model,

$$\begin{aligned} S_\nu = \frac{1}{J}\Bigg[& \frac{1}{Re}\left[-\rho\left(c_{w1}f_w - \frac{c_{b1}}{\kappa^2}f_{t2}\right)\left(\frac{\tilde{\nu}}{d}\right)^2\right] \\ & + \frac{1}{Re}\left[\frac{\rho}{\sigma}c_{b2}(\nabla\tilde{\nu})^2 - \frac{1}{\sigma}(\nu + \tilde{\nu})\nabla\tilde{\nu} \bullet \nabla\rho\right] \\ & + Re[\rho f_{t1}(\Delta q)^2] + \rho c_{b1}(1 - f_{t2})\tilde{S}\tilde{\nu}\Bigg] \end{aligned} \tag{6}$$

Other auxiliary relations and coefficients for the SA turbulence model can be found in [28,58].

B. Navier–Stokes Equations Solver

The in-house high-order CFD code Flow-Acoustics-Structure Interaction Package (FASIP) is used to solve the two-dimensional URANS equations. A third-order Weighted Essentially Non-Oscillatory (WENO) scheme for the inviscid flux [59–64] and fourth-order central differencing for the viscous terms [60,64] are employed to

discretize the Navier–Stokes equations. The low-diffusion E-CUSP scheme suggested by Zha et al. [61] based on the Zha–Bilgen flux vector splitting [65] is used with the WENO scheme to evaluate the inviscid fluxes. All the simulations in this study are conducted as unsteady time-accurate simulations. The second-order time-accurate implicit method with pseudotime and Gauss–Seidel line relaxation is used to achieve a fast convergence rate [59,66]. Parallel computing is implemented to save wall-clock simulation time [66,67]. The numerical results are time-averaged results after the flows and all the aerodynamic forces become dynamically stable. The FASIP code is intensively validated for CFWJ simulations [22–25,27,29,67–72]. Particularly, the predicted power coefficient P_c of CFWJ agrees very well with the experiment [24], which provides a solid support for the energy prediction in the present study. Rumsey [51] compared different turbulent models for the NASA hump simulation. The SA one-equation model performs reasonably well to predict the surface pressure distribution, separation onset, and separation bubble length. It behaves as well as other Reynolds-averaged Navier–Stokes (RANS) models such as the Shear Stress Transport (SST) model.

III. NASA Hump

The NASA hump is widely used as a benchmark case to validate numerical algorithms and turbulence modeling [51] for flow control. The baseline hump configuration with no flow control is designed to have a converging section followed by a rapid area expansion downstream of the throat as shown in Fig. 3, which creates a severe diffusion and large flow separation.

To provide the pressure gradient distribution information of the NASA hump when the separation is removed after applying flow control, an inviscid simulation of the hump that has no flow separation is conducted. Figure 4 presents the Mach number contours on the left and the pressure coefficient C_p and pressure gradient $\partial p/\partial x$ distributions on the right with the mesh refinement results showing the mesh independent solutions. The region of the FPG is from 30 to 65%c, and the APG is from 65 to 80%c.

The viscous flow of the baseline geometry is simulated with an initial mesh of $408 \times 108 = 44{,}064$ cells. The mesh topology and boundary condition setup following Ref. [51] are discussed in Ref. [38]. Figure 5a is the Mach number contours displaying a large flow separation downstream of the baseline hump. Figure 5b gives the corresponding C_p and $\partial p/\partial x$ distributions of the viscous results. The present numerical simulation is in a very good agreement with the experiment for the C_p distribution and separation onset location at $x/C = 66.3\%$. The measured onset point in the experiment is at 66.5%c. The predicted separation onset location is determined using the skin friction distribution presented in Ref. [38]. The mesh refinement study is also conducted by doubling the grid points in both directions. The reattachment point is slightly overpredicted as reported by other research groups using RANS models [51,73]. The mesh refinement study indicates that the solutions are converged based on the initial mesh size. The unsteady simulation uses a constant nondimensional characteristic time step $\Delta\bar{t} = 5 \times 10^{-3}$ with the maximum L2-norm residual typically reduced by two orders of magnitude within less than 40 pseudotime iterations per physical time step. Details of the residual convergence histories are presented in Ref. [38].

Two experimental cases with active flow control are used to validate the present numerical simulation [38], steady injection [54], and steady suction cases [51]. The steady injection case validates the CFWJ injection simulation, and the steady suction case validates the CFWJ suction prediction. The numerical validation results agree well with the experiments for both cases in terms of flowfield structures (e.g., separation mitigation) and C_p distribution. To avoid redundancy and save space, the details of those validations are not presented in this paper and can be found in Ref. [38].

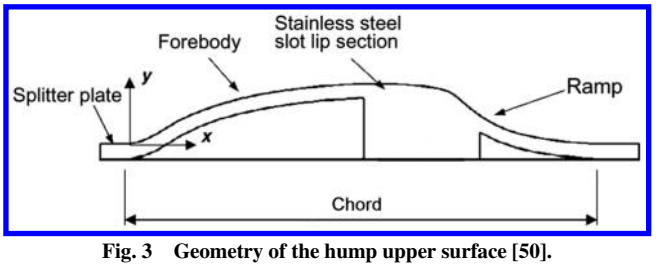

Fig. 3 Geometry of the hump upper surface [50].

IV. Coflow Wall Jet Hump

A. CFWJ Hump Geometry

The CFWJ hump configurations are created as described in Ref. [38] and are illustrated in Fig. 6. The surface between the injection and suction slots is slightly moved downward by 0.1%c to facilitate the tangential injection of the coflow wall jet.

Similar to a CFWJ airfoil, Fig. 6 (middle plot) shows that a small amount of mass flow is drawn into the hump downstream, pressurized and energized by a microcompressor pumping system inside the hump, and ejected through the upstream injection slot tangential to the main flow. In the present simulation, the microcompressor actuator is simulated by applying the total pressure inlet boundary condition (BC) at the injection slot and static pressure outlet BC at the suction slot as shown in the bottom plot of Fig. 6. The calculation has two layers of iterations: 1) matching the specified C_μ and 2) matching the suction mass flow rate to the injection one for ZNMF. This method is validated in the previous work [22–25,27–29,48,68–72].

As indicated in Ref. [38], it is effective to suppress flow separation by applying flow control near the separation onset point in adverse pressure gradients. Because CFWJ has both the injection and suction simultaneously, the present research will have the cases with either

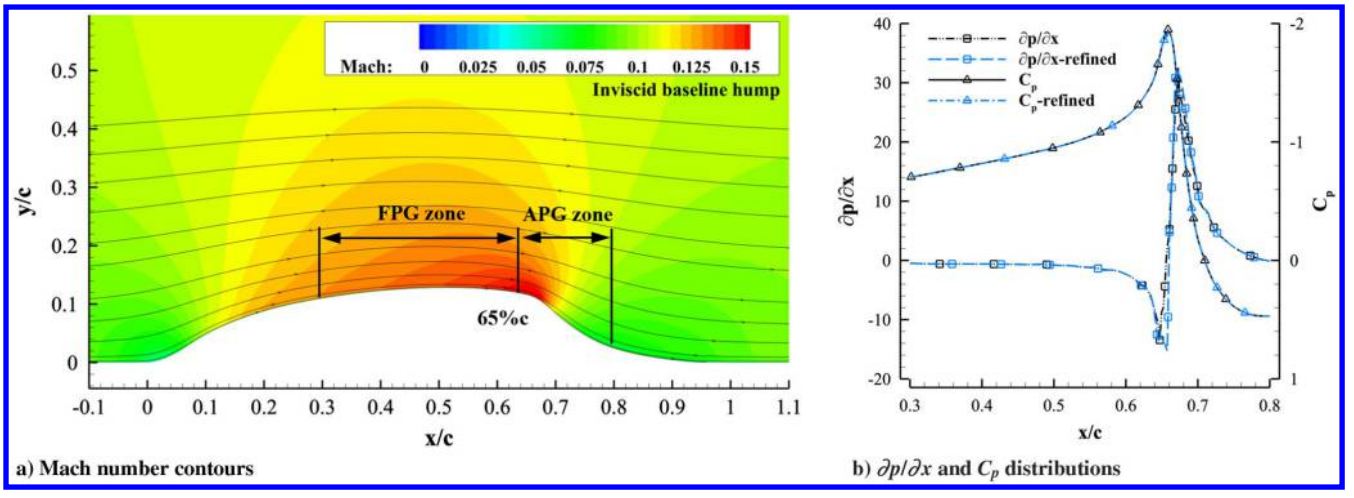

Fig. 4 Results of the baseline hump with inviscid flow simulation.

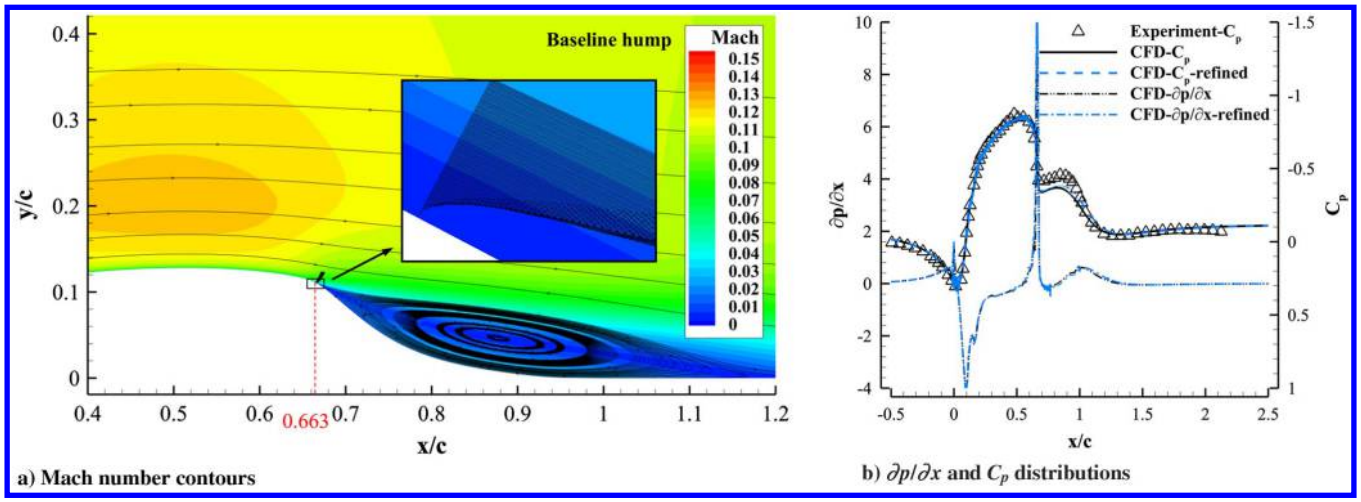

Fig. 5 Results of the viscous baseline hump.

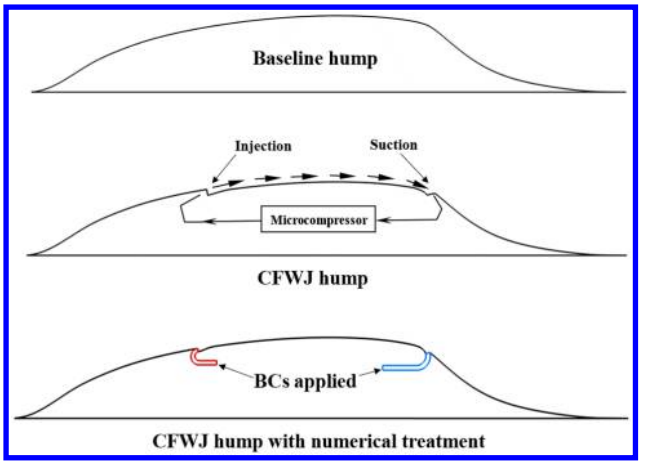

Fig. 6 Sketch of the CFWJ hump.

the injection or suction placed at the separation onset point to study their individual effect. CFWJ is devised to place the suction downstream and injection upstream. When the suction slot is placed near the separation onset point, the injection has to be located upstream with the favorable pressure gradient. Based on the regions with favorable pressure gradients (FPG) and adverse pressure gradients (APG) indicated in Fig. 4, the present study hence has two categories of pressure gradients that the injection slot is located: 1) the adverse pressure gradient when the injection is placed near the separation onset point and 2) the favorable pressure gradient when the suction is placed near the separation onset point.

Even though this paper primarily studies the injection and suction location effect, the slot size of injection and suction also plays a very important role in energy expenditure. McGahan [74] observed that a larger size of the wall jet injection slot reduces more energy consumption. But there is an optimized slot size. Our studies agree with McGahan's observation [24,28,41,47]. The reason is that a larger injection slot size will reduce the jet velocity and total pressure loss of the CFWJ, which requires a lower total pressure ratio of the microcompressors. As explained by Eq. (1), the CFWJ power required is determined exponentially by the total pressure ratio. However, the injection slot size should not be too large to lose the required jet momentum. The slot size for this study is already optimized based on our previous experience. Thus, the focus of the trade study is on the injection and suction slot location to investigate their effect on energy expenditure in different pressure gradients.

B. Injection in Adverse Pressure Gradients

The slot sizes of 0.5%c for injection and 0.7%c for suction are adopted for all the cases. The C_μ of 0.85% is used for all the cases because this is the minimum value that makes one of these cases fully attached. The purpose is to compare the behavior of different CFWJ location effects with the same injection strength.

1. *Injection Location Trade Study*

The CFWJ configurations with injection located at 65, 67.5, and 70%c shown as cases 1, 2, and 3 in Fig. 7 are first studied. The suction slot is fixed at 90%c location for all these cases. Among the three injection locations, the 67.5%c is the closest to the separation onset location of 66.5%c. The injection slots at 65 and 70%c are not drawn in Fig. 7 but are indicated by the arrows for the clarity of the plot.

Figure 8 shows the Mach number contours of the injection location trade study with C_μ of 0.85%. Flow separation is observed for case 1 downstream of the injection located at 65%c. As the injection location is moved to 67.5%c for case 2, 1%c downstream of the separation onset point, flow is fully attached. Placing the injection at the 65%c is still able to remove the flow separation but needs to increase the C_μ to 1.7%, 100% higher than 0.85%. Case 3 with the injection located at 70%c always has a small separation upstream of the injection slot, which is not able to be removed even with a very large C_μ.

Table 1 compares the power consumption of the two APG CFWJ injection cases that are able to remove the separation with their respective minimum required C_μ. Case 3 with the injection at 70%c is not included because it is unable to remove the small flow separation upstream of the injection slot. The $\dot{\bar{m}}$ is the normalized CFWJ mass flow rate, defined as $\dot{m}/(\rho_{\text{ref}} U_{\text{ref}} A_{\text{ref}})$, and Γ is the total pressure ratio between CFWJ injection and suction. The Re_h is the Reynolds

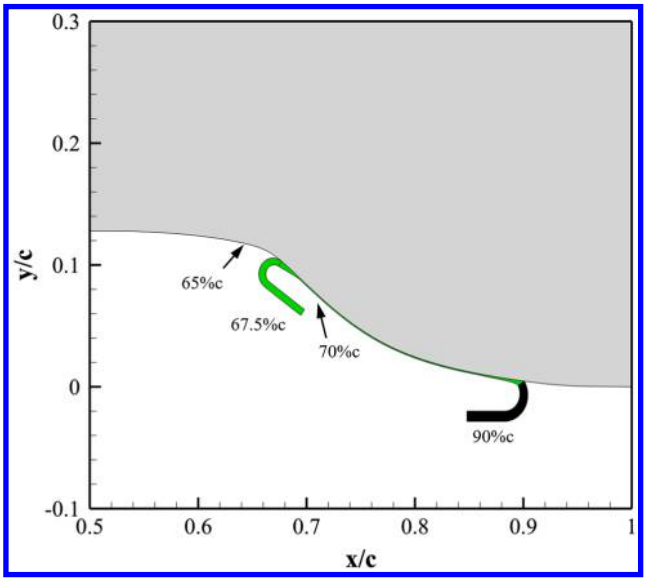

Fig. 7 Injection location trade study (cases 1, 2, 3).

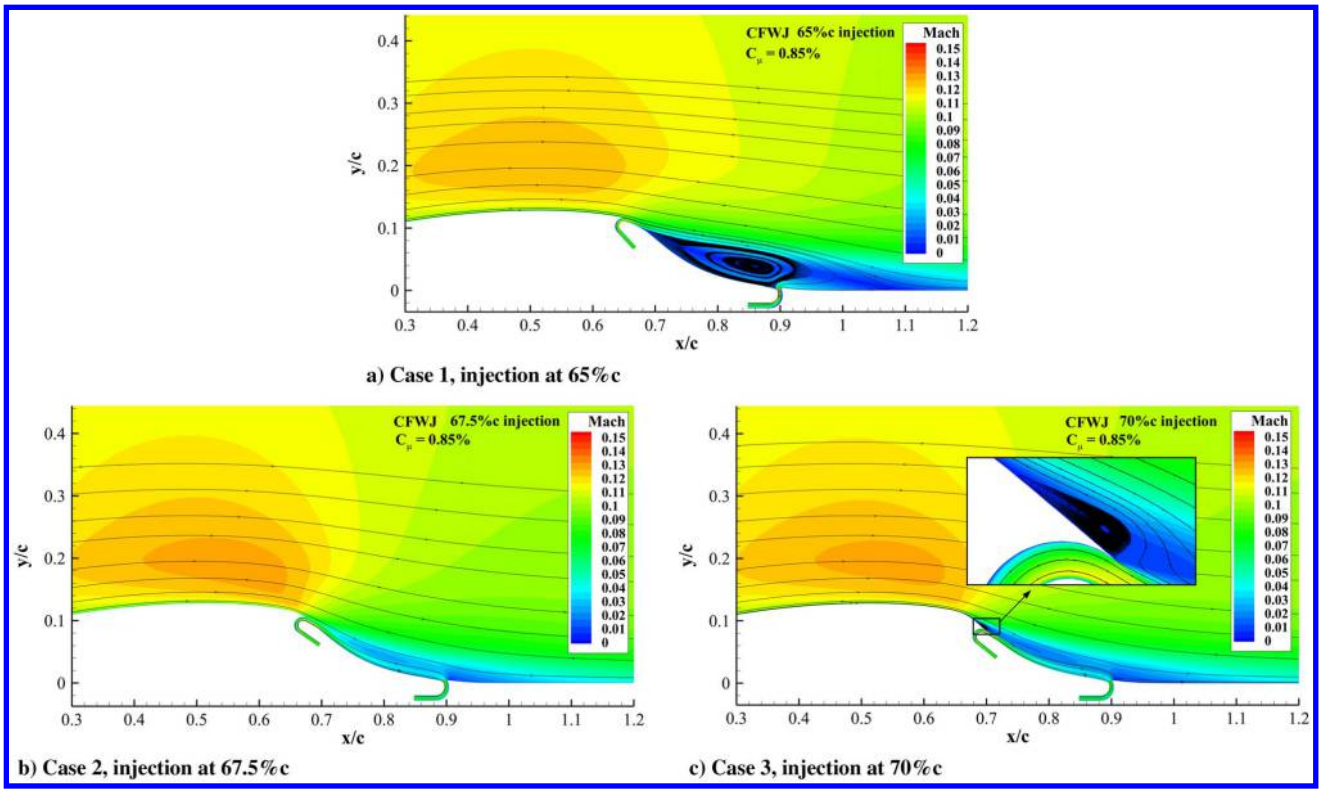

Fig. 8 Injection location trade study with the suction fixed at 90%c position.

Table 1 Power consumption of cases 1 and 2 with APG injection

Cases	Inj, %c	Suc, 5c	C_μ, %	Re_h	$U_{\text{jet}}/U_{\text{ref}}$	P_c	$\bar{\dot{m}}$, %	Γ	Flow
CFWJ 1	65	90	1.70	6236	1.31	0.0060	0.65	1.0060	Fully attached
CFWJ 2	67.5	90	0.85	4379	0.92	0.0030	0.46	1.0045	Fully attached

Inj = Injection.
Suc = Suction.

number based on the injection slot height. The CFWJ power coefficient P_c of case 2 is 50% smaller than that of case 1. It indicates that placing the injection slightly downstream of the separation onset point is much more efficient than placing it upstream. The 50% power reduction is attributed to the 29% smaller mass flow rate, and the rest is attributed to the 0.15% smaller total pressure ratio, which indicates that a very small reduction of the total pressure ratio such as 0.15% can reduce the total pressure ratio term in Eq. (1) by 30% due to the exponential effect.

2. *Suction Location Trade Study*

Because the injection location at 67.5%c is the most efficient position for the injection trade study, the injection is thus fixed at 67.5%c and has the suction varied at four positions: 70, 75, 80, and 85%c (cases 4, 5, 6, and 7) as shown in Fig. 9. The suction at 70%c position is not drawn but is indicated by an arrow for the plot clarity.

Figure 10 shows the Mach number contours of suction location trade study cases 4, 5, 6, and 7. All these cases have the same C_μ of 0.85%. For case 4 with the suction at 70%c (Fig. 10a), the closest to the injection slot, large flow separation occurs. With the suction slot moved downstream to 75 and 80%c (Figs. 10b and 10c, cases 5 and 6), the flow separation is mostly removed with a tiny separation bubble that can only be observed when it is zoomed in. When the suction is located at 85%c (Fig. 10d, case 7), the flow separation is completely removed, the same as case 2 with the suction located at 90%c.

Figure 11 compares the normalized total pressure contours of case 5 with case 7 to show the energy transfer difference between the flow slightly separated and fully attached. Note all these suction trade study cases have the same injection strength, injection total pressure, injection location, and C_μ. For case 5 shown in Fig. 11a, the jet still has high energy when it is withdrawn into the suction slot because it does not have enough length to mix with the main flow and transfer the energy. The boundary layer is thus not energized enough to overcome the adverse pressure gradient and is slightly separated as

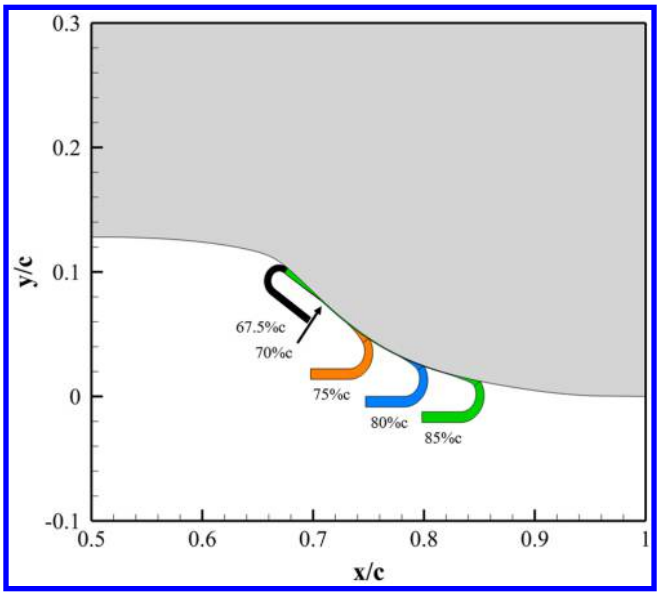

Fig. 9 Suction location trade study (cases 4, 5, 6, 7).

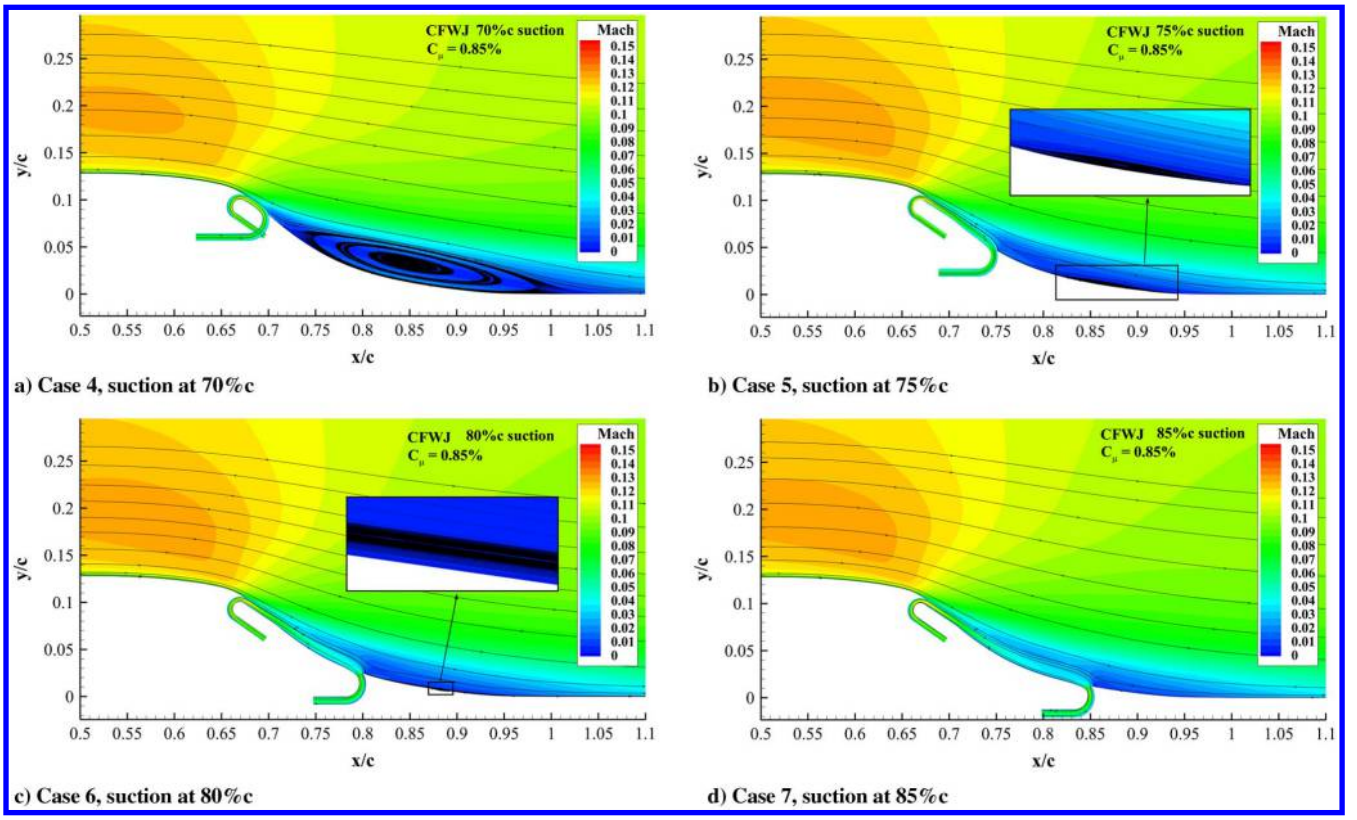

Fig. 10 Suction location trade study with the injection fixed at 67.5%c position.

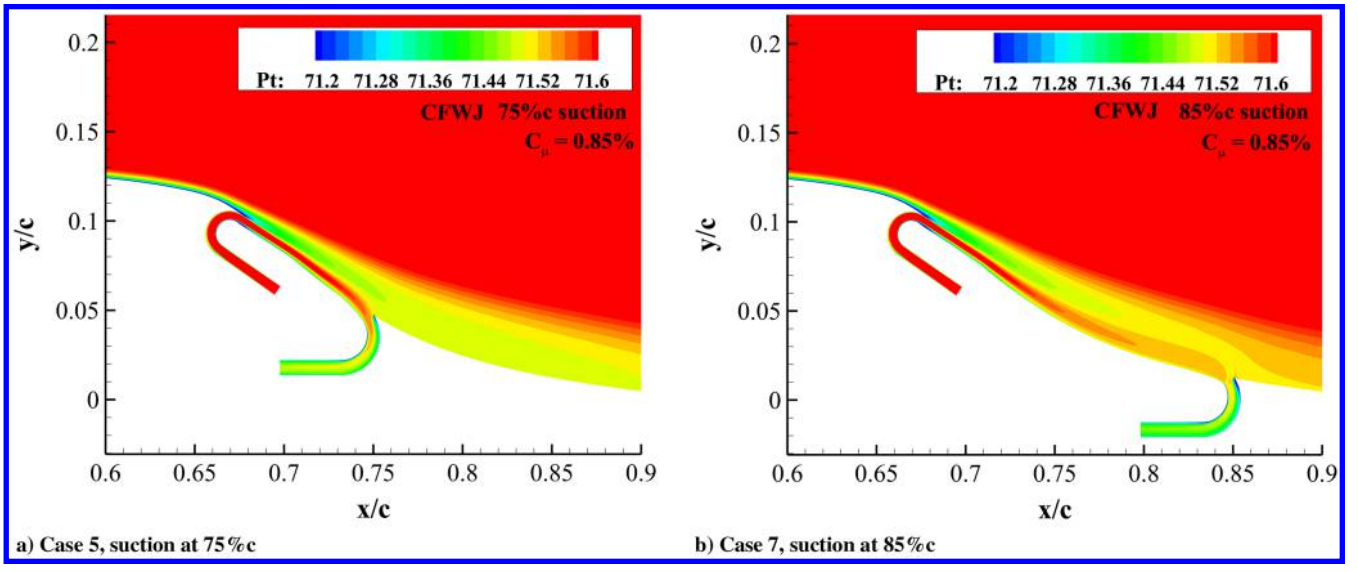

Fig. 11 Total pressure comparison with the injection fixed at 67.5%c.

shown in Fig. 10b. For case 7 as shown in Fig. 11b, a longer distance between the suction and injection slot makes the jet mixing more thoroughly. The lower total pressure at the suction slot is due to more energy transferred from the jet to the main flow boundary layer by mixing. In other words, a sufficiently long distance for mixing between the injection and suction of CFWJ is beneficial to suppress the flow separation.

The flow of cases 4, 5, and 6 can be fully attached when their corresponding C_μ is increased. Table 2 compares the power consumption for cases 4, 5, 6, and 7 with their minimum C_μ that attaches

Table 2 Power consumption of various suction location cases with APG injection

Cases	Inj, %c	Suc, %c	C_μ, %	Re_h	$U_{\text{jet}}/U_{\text{ref}}$	P_c	$\dot{\bar{m}}$, %	Γ	Flow
CFWJ 2	67.5	90	0.85	4379	0.92	0.0030	0.46	1.0045	Fully attached
CFWJ 4	67.5	70	3.00	8216	1.73	0.0110	0.86	1.0090	Fully attached
CFWJ 5	67.5	75	1.00	4760	1.00	0.0034	0.50	1.0048	Fully attached
CFWJ 6	67.5	80	0.90	4512	0.95	0.0032	0.47	1.0048	Fully attached
CFWJ 7	67.5	85	0.85	4379	0.92	0.0030	0.46	1.0046	Fully attached

the flow. With the suction slot moved downstream from 70 to 85%c, the C_μ that is able to attach the flow is substantially decreased by 72% from C_μ of 3 to 0.85%. The CFWJ power is dropped by a similar amount of 73%. For case 7 and case 2, the only difference is that the suction is at 85%c for the former and at 90%c for the latter (Table 2). They have the same CFWJ power coefficient P_c of 0.0030. In this case, the injection close to the separation onset point has the dominant effect. The suction has a weak coupling effect to suppress the flow separation but mainly serves as the flow source to achieve ZNMF.

Three conclusions may be drawn from these trade study results with CFWJ APG injection: 1) The injection of CFWJ placed slightly downstream of the separation onset point is most effective and efficient to remove flow separation in adverse pressure gradients.

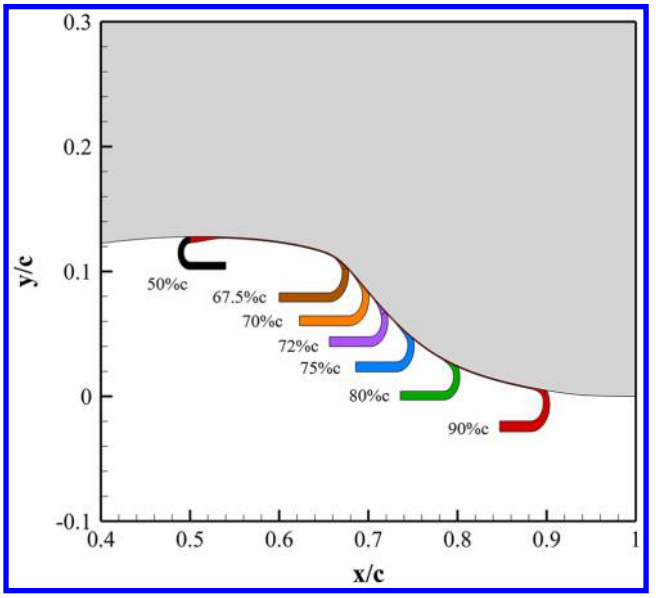

Fig. 12 Suction location trade study (cases 8–13).

2) The distance between the injection and suction slot needs to be long enough so that the CFWJ can be fully mixed with the main flow to transfer the energy. 3) When the injection is located at the desirable position slightly downstream of the separation onset point and the mixing distance is sufficiently long, the injection effect is dominant, and the suction has a weak coupling effect but primarily serves to withdraw the mass flow as the source for the injection.

C. Injection in Favorable Pressure Gradients

When the CFWJ suction is placed near the separation onset location, the CFWJ injection will be placed upstream in the region of the favorable pressure gradient. This section is to conduct the trade study with the injection located in the FPG region. Similar to the last section, the trade study also consists of two parts: injection and suction location studies. The slot size of 0.5%c for injection and 0.7%c for suction and C_μ of 0.77% are used for all the cases.

1. Suction Location Trade Study

Figure 12 shows the various suction locations for the trade studies: cases 8, 9, 10, 11, 12, and 13, which have the injection location fixed at the FPG position of 50%c and the suction varied in the region of APG at 67.5, 70, 72, 75, 80, and 90%c.

For case 8 with the suction located at 67.5%c, the flow is slightly separated as shown in Fig. 13a. With the suction moved to 70%c location (Fig. 13b) for case 9, the flow is fully attached. If the suction location is moved 2%c farther downstream to 72%c for case 10, a large flow separation occurs at 0.65 X/C 1.15. Further moving the suction slot downstream to 75, 80, and 85%c results in a large flow separation as for the 72%c location and is not shown. These results support the analysis in Ref. [38] that applying a flow control such as a suction close to the separation onset point is effective to suppress the flow separation. However, the criterion to determine the optimal distance placing a flow control actuation downstream of the separation onset point remains to be studied.

Referring to Fig. 13, Fig. 14 compares the velocity profiles for case 8 (mildly separated) and case 9 (fully attached) with the same C_μ of

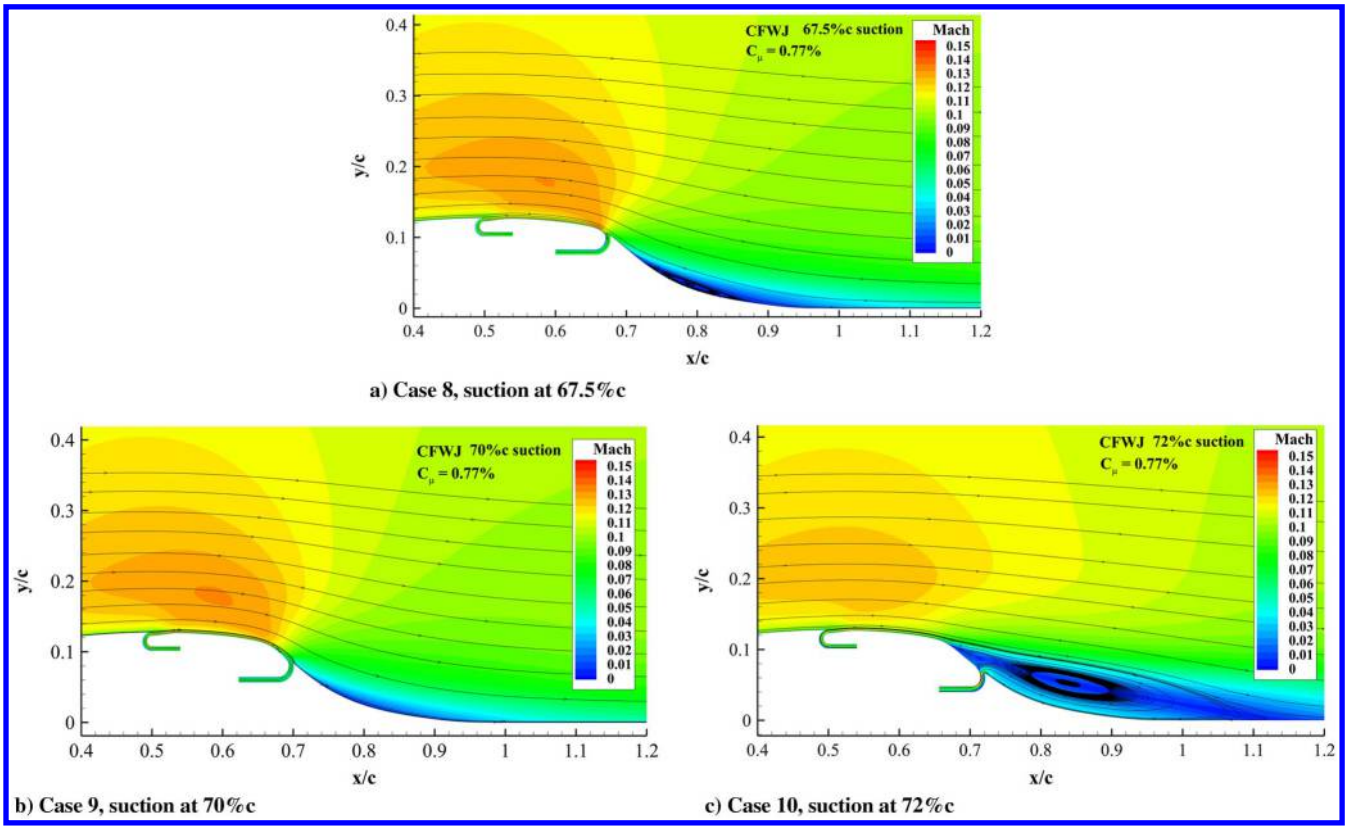

Fig. 13 Suction location trade study with the injection fixed at 50%c.

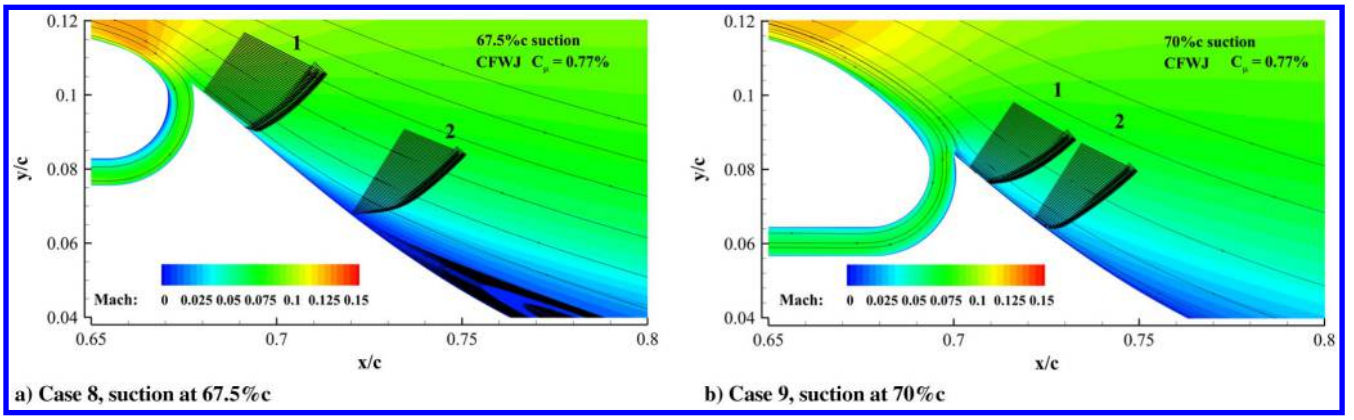

Fig. 14 Mach number contours and velocity profiles.

0.77% at a location immediately downstream of the suction slot (station 1) and a common location at 72%c (station 2). Case 8 has a much stronger boundary layer profile immediately downstream of the suction slot than case 9. However, the momentum is quickly dissipated, and the boundary layer is weaker than that of case 9 at the location of 72%c. This is because the suction is not far enough from the injection to provide sufficient distance to energize the boundary layer via mixing. The jet is withdrawn into the suction slot too early and is still in a high-energy state. The suction location at 70%c of case 9 provides a longer distance to make full use of the kinetic energy from the injection. Table 3 quantifies the displacement thickness δ^* and shape factor H of the boundary layer profile at stations 1 and 2 for cases 8 and 9, respectively. At station 1, case 8 has a healthier boundary layer profile than case 9 in terms of smaller displacement thickness δ^* and H factor. However, as the flow travels downstream to station 2, the H factor and δ^* of case 8 increase dramatically and exceed those of case 9.

For cases 8 and 10 with flow separation shown in Fig. 13, the flow can be attached by increasing C_μ. Table 4 lists the results with their corresponding minimum C_μ that makes the flows attached with the injection fixed at 50%c. A significant difference of the suction location trade study from the injection trade study in Sec. IV.B is that all cases with different suction locations including the one at deep separation region of 90%c can attach the flow, but at a high energy cost as shown in Table 4. The most effective injection location at APG from the trade study in Sec. IV.B is downstream of the baseline separation onset point at 67.5%c. However, as shown in Table 4 for case 8, placing the suction at this location has the C_μ and P_c increased by 69 and 109%, respectively, compared with placing it at 70%c. In other words, placing the injection or suction slot slightly downstream of the separation onset point is the most effective for separation removal. But the desirable suction location is a little downstream of the optimal injection location. Note that the optimal location herein refers to the most effective location based on the current hump configurations and the limited trade study cases. The quantitative results should not be generalized and are not conclusive.

Table 4 indicates that case 9 with the suction location at 70%c is the optimum among the cases of the suction location trade study. Placing the suction upstream or downstream of this location consumes more energy.

2. Injection Location Trade Study

For the injection location study as illustrated in Fig. 15, three locations of 30, 60, and 65%c (cases 14, 15, and 16) in the FPG area are simulated with suction fixed at 70%c, which is the optimal suction location from case 9. The injection at 65%c is not plotted in Fig. 15 but is indicated by an arrow for clarity.

Figure 16 shows the Mach number contours of the CFWJ hump at injection locations of 30, 60, and 65%c with $C_\mu = 0.77\%$. Case 14 with injection at 30%c is able to completely remove the separation. Cases 15 and 16 with injection located more downstream closer to the suction slot have flow separation that occurred due to the insufficient mixing distance, which is the same reason as for cases 4, 5, and 6.

Table 5 compares the energy consumption of the trade study of FPG injection cases. All cases in Table 5 use the minimum C_μ that makes the respective flow fully attached. Comparing cases 14 and 15, case 15 has the C_μ and mass flow rate increased by 47 and 23%, respectively, but the power coefficient is reduced by 2.6%. It is because the total pressure ratio of case 15 is 0.1% lower than that of case 14 as explained by Eq. (1). However, both cases 14 and 15 have a higher P_c than case 9 that has the injection location at 50%c with a P_c of 0.0032. Case 9 has the injection located between that of cases 14 and 15. It combines the advantages of the low mass flow rate of case 14 and the low total pressure ratio of case 15. It thus has the minimum CFWJ power coefficient. Case 9 is therefore regarded as the optimum of the FPG injection CFWJ.

Table 3 Details of velocity profiles of cases 8 and 9

		Station 1		Station 2	
Cases	C_μ	δ^*	H	δ^*	H
CFWJ 8	0.77%	2.6×10^{-3}	1.18	1.35×10^{-2}	1.96
CFWJ 9	0.77%	8.84×10^{-3}	1.58	1.21×10^{-2}	1.66

D. Comparison of Optimal Cases with Injection in APG and FPG

Figure 17 compares the minimum power coefficients P_c for all the trade study cases with the flow fully attached. Case 3 that is not able to fully attach flow is omitted in the plot. The solid square symbol represents the injection location studies in APG (cases 1 and 2, Table 1), the solid triangle symbol represents the suction location studies with the injection in APG (cases 4–7, Table 2), the open

Table 4 Power consumption of various suction location cases with FPG injection

Cases	Inj, %c	Suc, %c	C_μ, %	Re_h	$U_{\text{jet}}/U_{\text{ref}}$	P_c	$\dot{\bar{m}}$, %	Γ	Flow
CFWJ 8	50	67.5	1.30	5474	1.15	0.0067	0.56	1.008	Fully attached
CFWJ 9	50	70	0.77	4189	0.88	0.0032	0.44	1.005	Fully attached
CFWJ 10	50	72	1.40	5664	1.19	0.0080	0.59	1.009	Fully attached
CFWJ 11	50	75	1.75	6283	1.32	0.0110	0.66	1.012	Fully attached
CFWJ 12	50	80	2.10	6902	1.45	0.0160	0.72	1.015	Fully attached
CFWJ 13	50	90	2.30	7187	1.51	0.0170	0.75	1.016	Fully attached

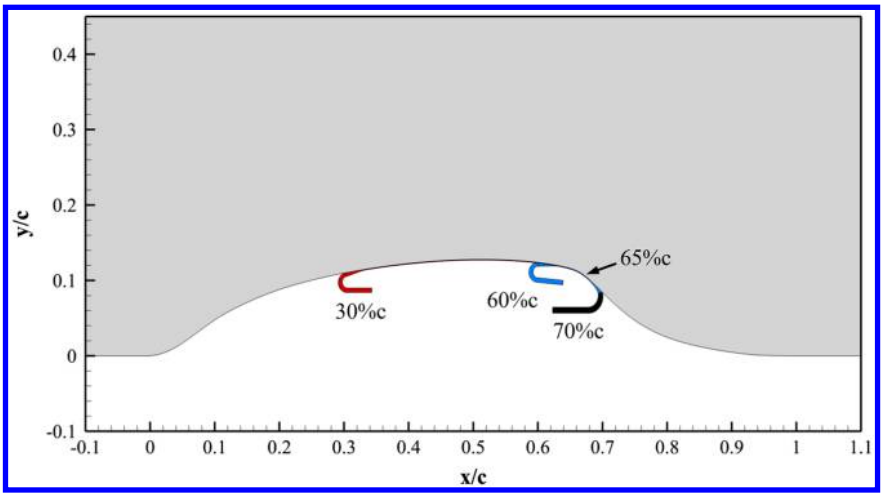

Fig. 15 Injection location trade study (cases 14, 15, and 16).

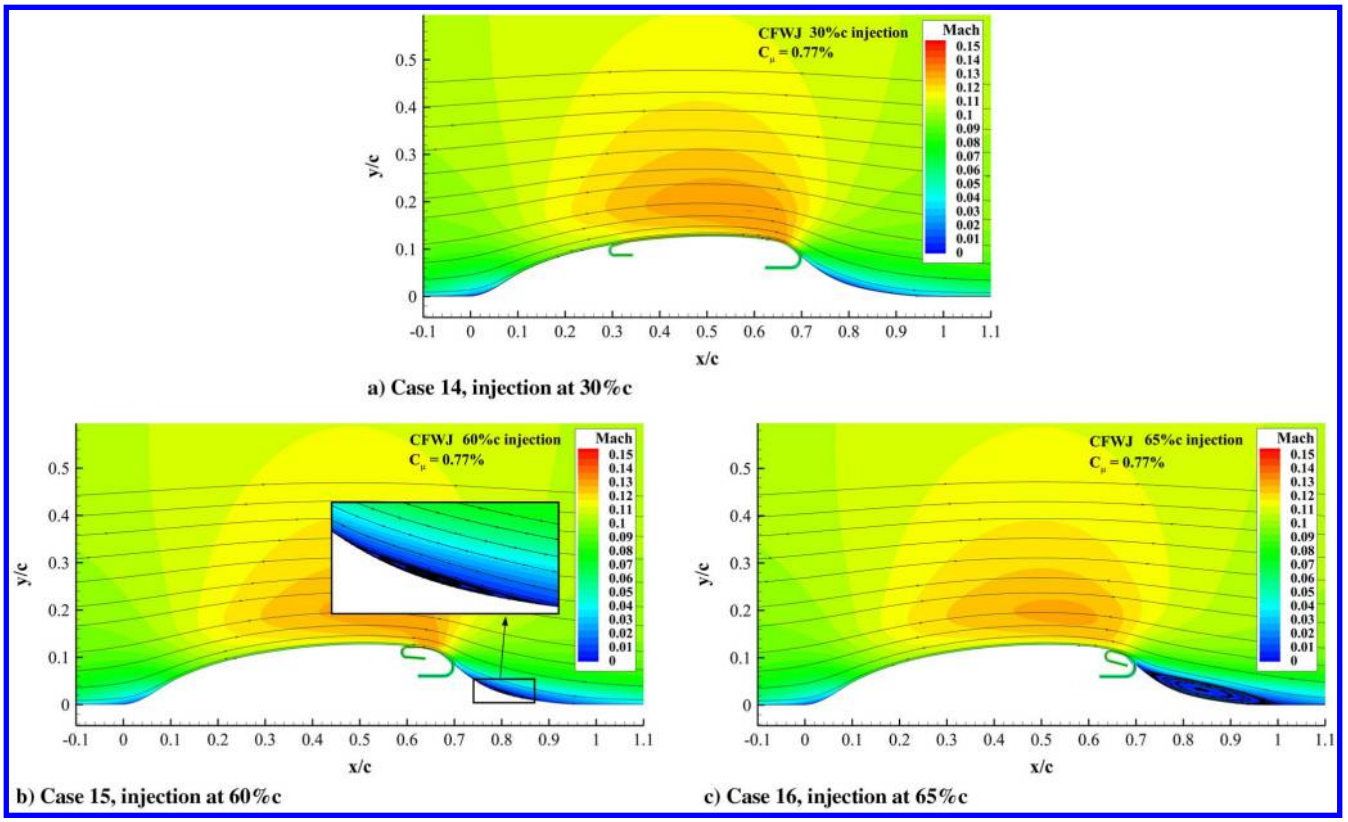

Fig. 16 Injection location trade study with the suction fixed at 70%c.

diamond symbol represents the suction location studies with the injection in FPG (cases 8–13, Table 4), and the open circle symbol represents the injection location studies in FPG (cases 14–16, Table 5). Figure 17 indicates that the minimum P_c is achieved by cases 2 and 9 that have their injection or suction located near the separation onset location and slightly downstream. It also shows that the optimal suction location (case 9) is a little more downstream than that of the optimal injection location (case 2).

Since cases 2 and 9 are the two most efficient cases, investigation of the flow structure difference between them is useful to understand the effect of injection in APG (case 2) and injection in FPG (case 9). Figure 18b shows the C_p distributions of the computed baseline NASA hump, cases 2 and 9 compared with that of the baseline with no flow control. The pressure reaches the lowest value at the negative C_p peak location and immediately experiences a sharp rise due to the rapid area expansion with the attached flow, which forms the pressure

Table 5 Power consumption of various injection location cases with FPG injection

Cases	Inj, %c	Suc, %c	C_μ, %	Re_h	$U_{\text{jet}}/U_{\text{ref}}$	P_c	$\bar{\dot{m}}$, %	Γ	Flow
CFWJ 9	50	70	0.77	4189	0.88	0.0032	0.44	1.005	Fully attached
CFWJ 14	30	70	0.75	4142	0.87	0.0039	0.43	1.006	Fully attached
CFWJ 15	60	70	1.10	5046	1.06	0.0038	0.53	1.005	Fully attached
CFWJ 16	65	70	1.90	6616	1.39	0.0059	0.59	1.006	Fully attached

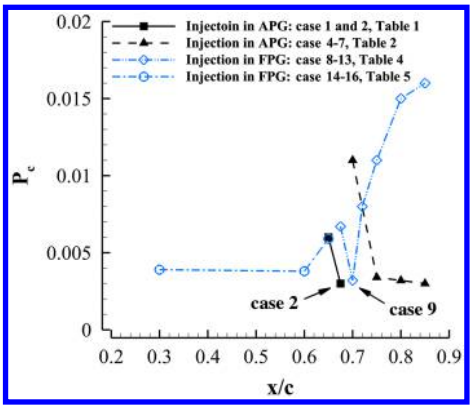

Fig. 17 Power coefficient vs locations.

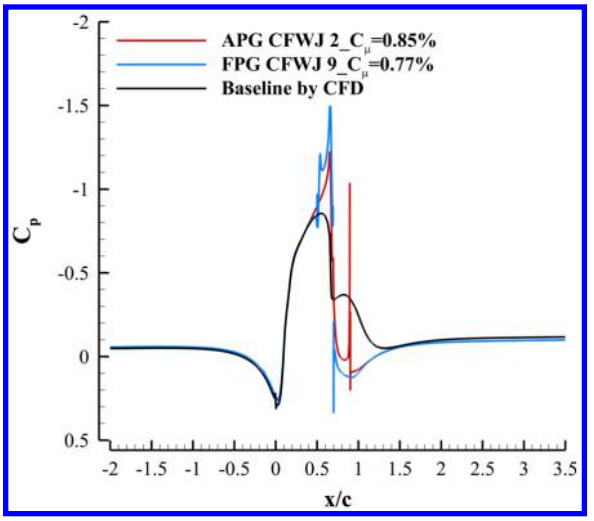

Fig. 18 C_p distributions for the baseline and the optimum CFWJ cases.

spikes at about 66%c. The sharp peak spike is also observed in the inviscid results as shown in Fig. 4b and also measured in the experiment when the flows are attached [38,51,54]. The C_p distribution of the two CFWJ cases are very similar, but case 9 has a higher suction peak and lower pressure valley than case 2, which indicates that case 9 experiences a greater acceleration and deceleration (diffusion) than that of case 2. Such a larger velocity variation of case 9 creates more energy loss and needs higher CFWJ power, as indicated in Table 6.

The C_p distribution has a pressure glitch caused by the numerical resolution at the hump leading edge of 0%c. This is due to the sharp change of the pressure caused by an abrupt geometry slope at the hump leading edge, which is not fully resolved by third-order WENO scheme. However, the minor glitch does not change the nature of the flowfield and energy analysis. The same numerical glitch is also reported by other researchers, including Rumsey [51], Koklu [55], and Uzun and Malik [75]. The rest of the pressure spikes are caused by the injection slots and suction slots for three reasons: 1) The pressure probes are along the wall surface without going into the ducts and skip the injection and suction slot opening. The pressure is not uniform across the injection and suction slot opening and appears as spikes when the pressure probe jumps from the injection slot lip to the hump surface and vice versa at the suction slot. 2) The injection and suction slot opening surface is a part of a control volume boundary for force integral and power required computation [24,27]. The slot opening surface is oriented to be approximately normal to the flow. The coordinates across the slot opening surface hence have a very small discontinuity as shown in Fig. 18. 3) The sharp lip of the suction slot creates a very small acceleration zone followed by a stagnation zone, around which the flow generates a rapid pressure decrease and increase shown as spikes.

For comparison convenience, the power coefficient results of cases 2 and 9 are extracted from Tables 1 and 4 and are presented here in Table 6.

Comparing the P_c of the optimum APG injection and the optimum FPG injection, the optimum FPG injection case 9 requires a P_c about 6.7% higher than the optimum APG injection case 2 but has a 10% lower C_μ. This is because case 9 has a higher total pressure loss that needs a greater total pressure ratio Γ even though its mass flow rate is lower. This also indicates that C_μ should not be used to represent the power consumption of AFC because a high C_μ does not mean a high power consumption. Furthermore, the quantitative values of C_μ and P_c are dramatically different. Using C_μ instead of P_c to represent the added equivalent drag would create misleading results.

Figure 19 compares the contours of entropy increase (from the inlet) and velocity magnitude (normalized by the inlet velocity) for cases 2 and 9. As shown in Figs. 19a and 19b, the APG injection case 2 has a significantly lower entropy increase than that of the FPG injection case 9 within the CFWJ region due to the lower main flow velocity and shear stress work [76,77]. For the FPG injection case 9, the injection jet has strong acceleration due to the favorable pressure gradient as shown in Fig. 19d, resulting in a high velocity in the CFWJ region and high energy loss. For case 2, the velocity in the CFWJ region is substantially lower than that of case 9 due to the severe adverse pressure gradient and flow diffusion as shown in Figs. 19c and 19d. The loss comparison of Fig. 19 is consistent with the coflow wall jet separation control analysis conducted in [38], which indicates that it is more efficient and effective to apply the coflow wall jet in the adverse pressure gradient region starting from the near-separation-onset location.

Figure 20 compares the spanwise vorticity contours for cases 2 with the injection in adverse pressure gradients (Fig. 20a) and case 9 with the injection in favorable pressure gradients (Fig. 20b). For case 2 with the CFWJ completely immersed in the APG region, the three counterrotating layers of vorticity are observed clearly downstream of the injection slot (Fig. 20a), a layer of clockwise vorticity due to the wall boundary layer in blue, a layer of counter-clockwise vorticity due to the wall jet in red, a zero-vorticity layer indicating a transition of vorticity direction in green, and a layer of clockwise vorticity due to the main flow boundary layer mixing with the wall jet in blue. With the CFWJ flowing downstream, it is observed that the wall jet counterclockwise vorticity layer is decayed and dissipated due to mixing and vanishes downstream at the suction slot where the CFWJ ends as shown in Fig. 20a. The vanishing of the counterclockwise wall jet vorticity appears to create a sufficient mixing distance to place the CFWJ suction for maximizing the efficiency in the adverse pressure gradient. Figure 20b shows the vorticity contours of the optimum FPG injection case 9, which has the three layers of counter-rotating vorticity layers thinner and shorter than those of case 2 in APG.

1. *Slots Effect with No Jets*

The sizes of the injection slot and suction slot are very small compared with the scale of the flowfield. They do not affect the flowfield in a notable way as observed in the experiment [28] when the jet is turned off. However, it may be possible that the tripping effect of the slots could help to attach the flow. If that is the case, the energy expenditure analysis would be inaccurately attributed to the CFWJ effect.

Table 6 Performance comparison of APG injection case 2 and FPG injection case 9

Cases	Inj, %c	Suc, %c	C_μ, %	Re_h	$U_{\text{jet}}/U_{\text{ref}}$	P_c	$\dot{\bar{m}}$, %	Γ	Flow
CFWJ 2	67.5	90	0.85	4379	0.92	0.0030	0.46	1.0045	Fully attached
CFWJ 9	50	70	0.77	4189	0.88	0.0032	0.44	1.0050	Fully attached

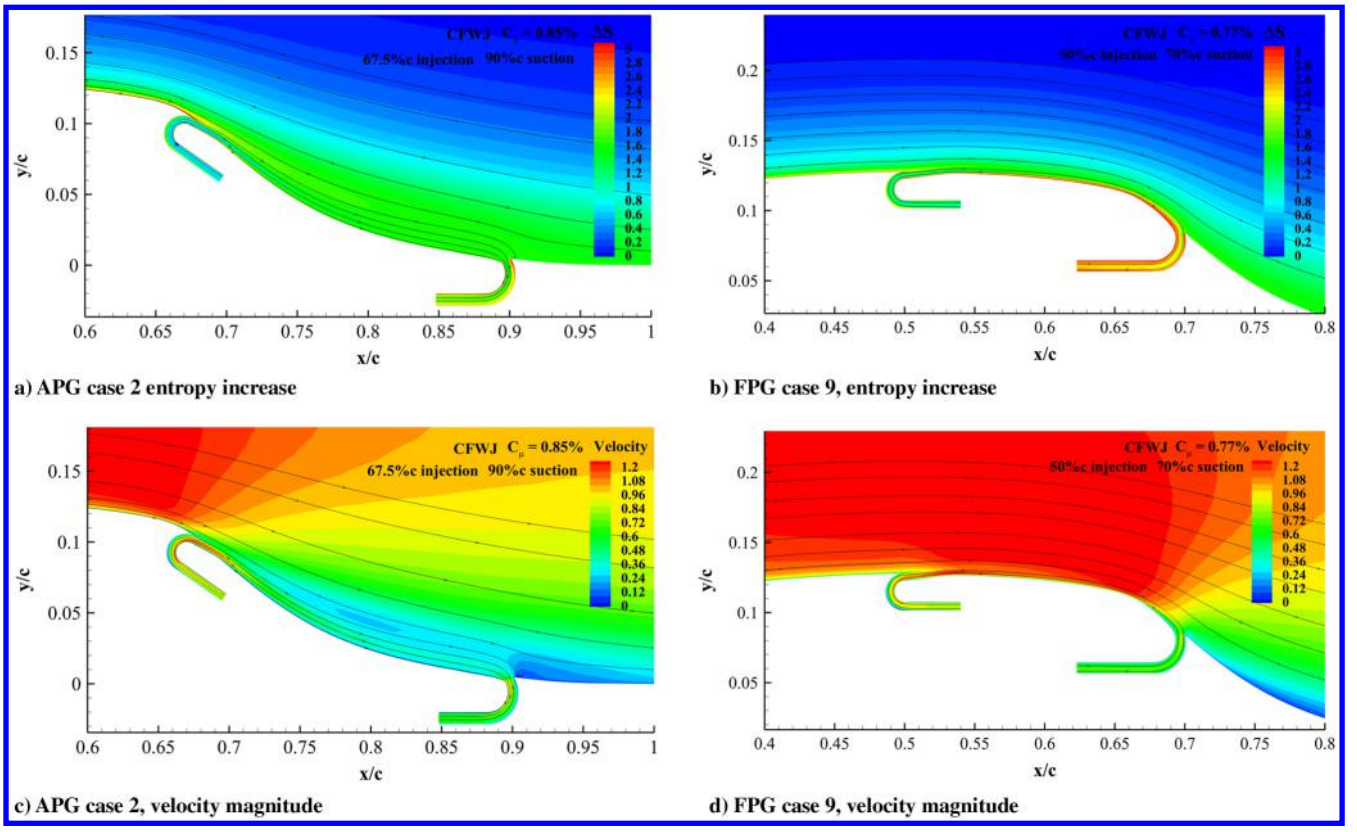

Fig. 19 Comparison between the optimum APG and FPG cases.

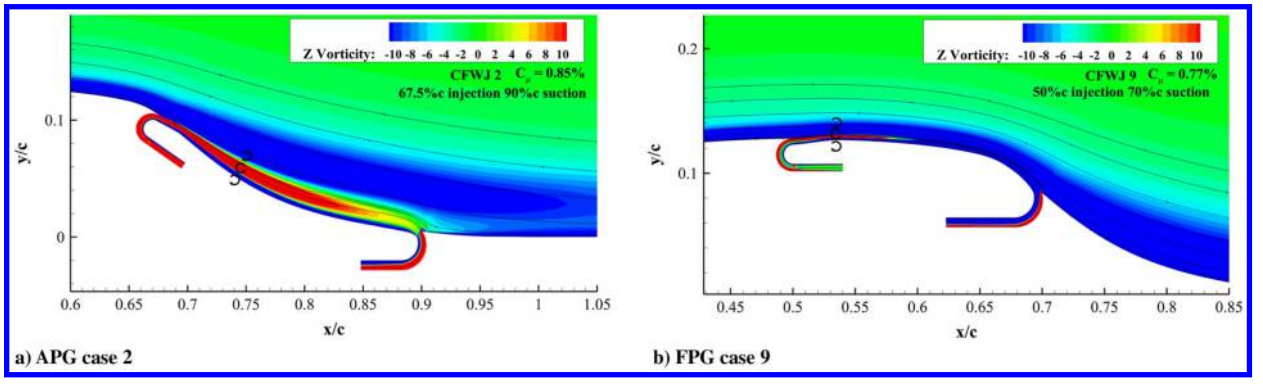

Fig. 20 Spanwise vorticity for the optimum FPG and APG cases.

To be certain that the slots of the CFWJ do not contribute to the flow attachment, the CFWJ cases 2 and 9 with no jets activated are simulated by sealing the injection inlet and suction outlet with no-slip wall boundary condition. The computed flowfields and flow separation patterns are virtually identical to those of the baseline flows shown in Fig. 5. This is evidenced by the surface C_p distributions of the CFWJ cases 2 and 9 with no jet compared with that of the baseline as shown in Fig. 21. They are basically the same except for the pressure spikes at 50 and 90%c locations due to the open-slot effects. These results indicate that the CFWJ slots without jets have no benefit to the separation control of this hump flow. The flow attachment is fully attributed to the CFWJ effect.

E. CFWJ Comparison with Injection-Only and Suction-Only Flow Control

To form a high-efficiency self-contained ZNMF system, the injection and suction are used together by the coflow wall jet. Other than satisfying the ZNMF role, it is important to answer the question raised in the Introduction whether there is a coupling effect of the injection and suction. In other words, is it more efficient and effective

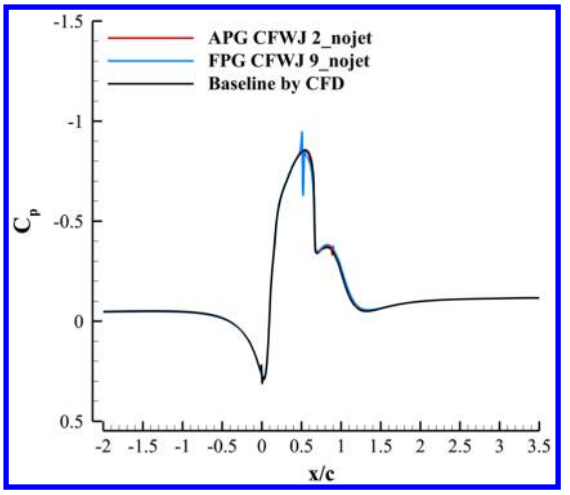

Fig. 21 C_p distributions for the baseline and the optimum CFWJ cases with no jet.

to use both injection and suction simultaneously than only to use injection or suction assuming ZNMF is not a concern? To answer these questions, the best way is to compare the effectiveness and efficiency of CFWJ and the AFC with only injection or suction. That is the purpose of this section.

1. *Injection-Only Flow Control*

To have a rigorous comparison, the C_μ, slot location, orientation, and sizes are kept the same as the two optimum CFWJ cases, cases 2 and 9 shown in Table 6. To study the injection slot effect, the approach is to simply remove the suction slots of cases 2 and 9 and use the same injection slots at 50 and 67.5%c (injection-only cases 1 and 2). As a trade study, one more injection location at 70%c (injection-only case 3) adopted from the CFWJ case 3 is added. Figure 22 shows the three injection locations of the injection-only cases 1, 2, and 3.

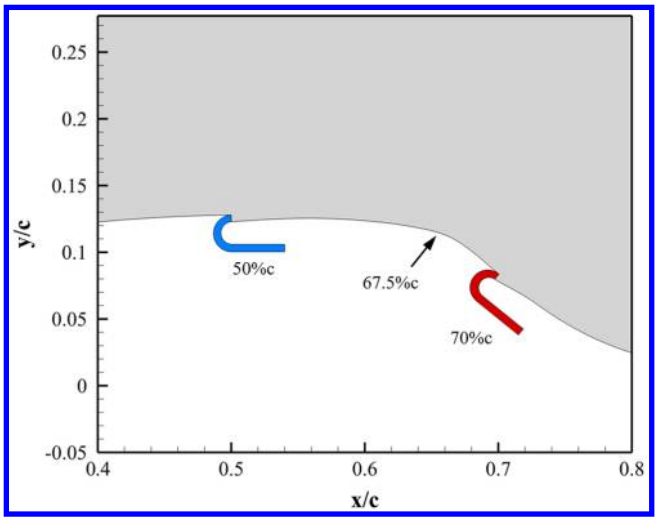

Fig. 22 Injection location trade study (injection-only cases 1, 2 and 3).

The injection-only case 2 is indicated by an arrow to make the figure clear. The C_μ of 0.85% from the CFWJ case 2 is used for all the injection-only cases for comparison.

Figure 23 shows the Mach number contours of the three injection-only cases. The injection location at 50%c is the same as the location of the optimum CFWJ case 9. However, without the downstream suction at 70%c as in the CFWJ case 9, the injection-only case has a large flow separation as shown in Fig. 23a even though the C_μ of 0.85% is higher than the C_μ of 0.77% of case 9. When the injection slot is moved to 67.5%c in Fig. 23b, the same location as that of case 2, a full flow attachment is achieved as the CFWJ case 2 with the same C_μ. Further moving the injection slot downstream to 70%c, a small flow separation occurs upstream of the injection slot as shown in Fig. 23c, which is similar to the CFWJ case 3 presented in Fig. 8.

Figure 24a shows the spanwise vorticity contours of the attached flow of the injection-only vase 2, which is very similar to the CFWJ vase 2 (with its suction slot shown by the dash lines in Fig. 24a) that has the same injection location. Figures 24b–24f also compare the velocity profiles (VPs) of the injection-only case 2 with those of the CFWJ case 2 and the baseline NASA hump at the same five streamwise stations labeled in Fig. 24a. The baseline NASA hump refers to the viscous results as shown in Fig. 5. At station 1, upstream of the injection slot at $x/h = -3$ as shown in Fig. 24b, the velocity profiles of the CFWJ case 2 and injection-only case 2 are already energized by the induction effect of the downstream injection and are significantly fuller with higher kinetic energy than the baseline case. Downstream of the injection slot at $x/h = 1$, the CFWJ case 2 and injection-only case 2 have almost identical wall jet VPs, which energize the boundary layer by mixing due to the high turbulent diffusion [38], whereas the baseline case is already separated with reversed velocities near the wall. As the flow reaches downstream to stations 3 and 4, the wall jet VPs are dissipated due to the jet mixing, and the VPs become typical turbulent boundary layer profiles. The CFWJ case 2 has a slightly higher velocity than the injection-only case 2 at station 4 due to the downstream suction effect at 90%c. From stations 4 to 5, the flow passes the suction slot, and the velocity profile of the injection-only

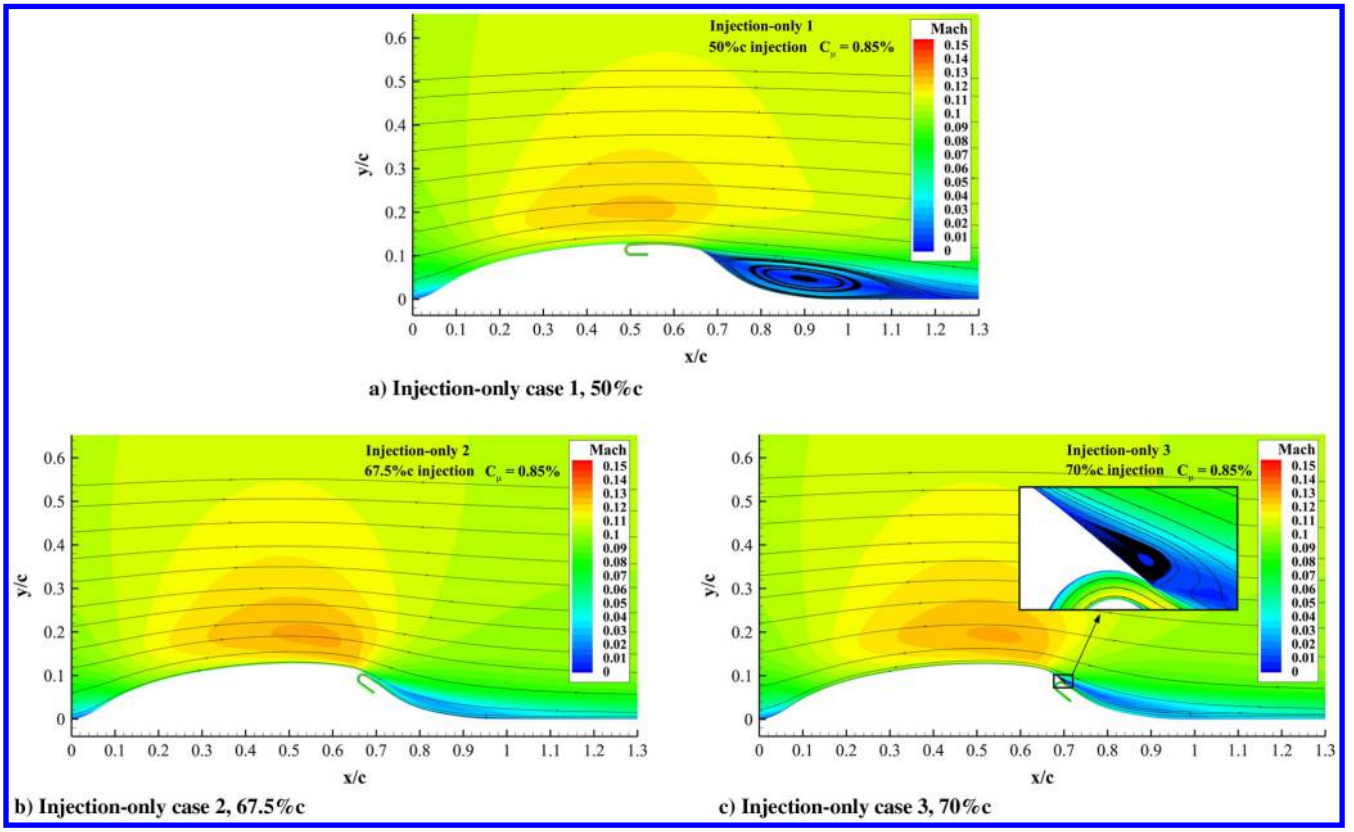

Fig. 23 Injection-only trade study.

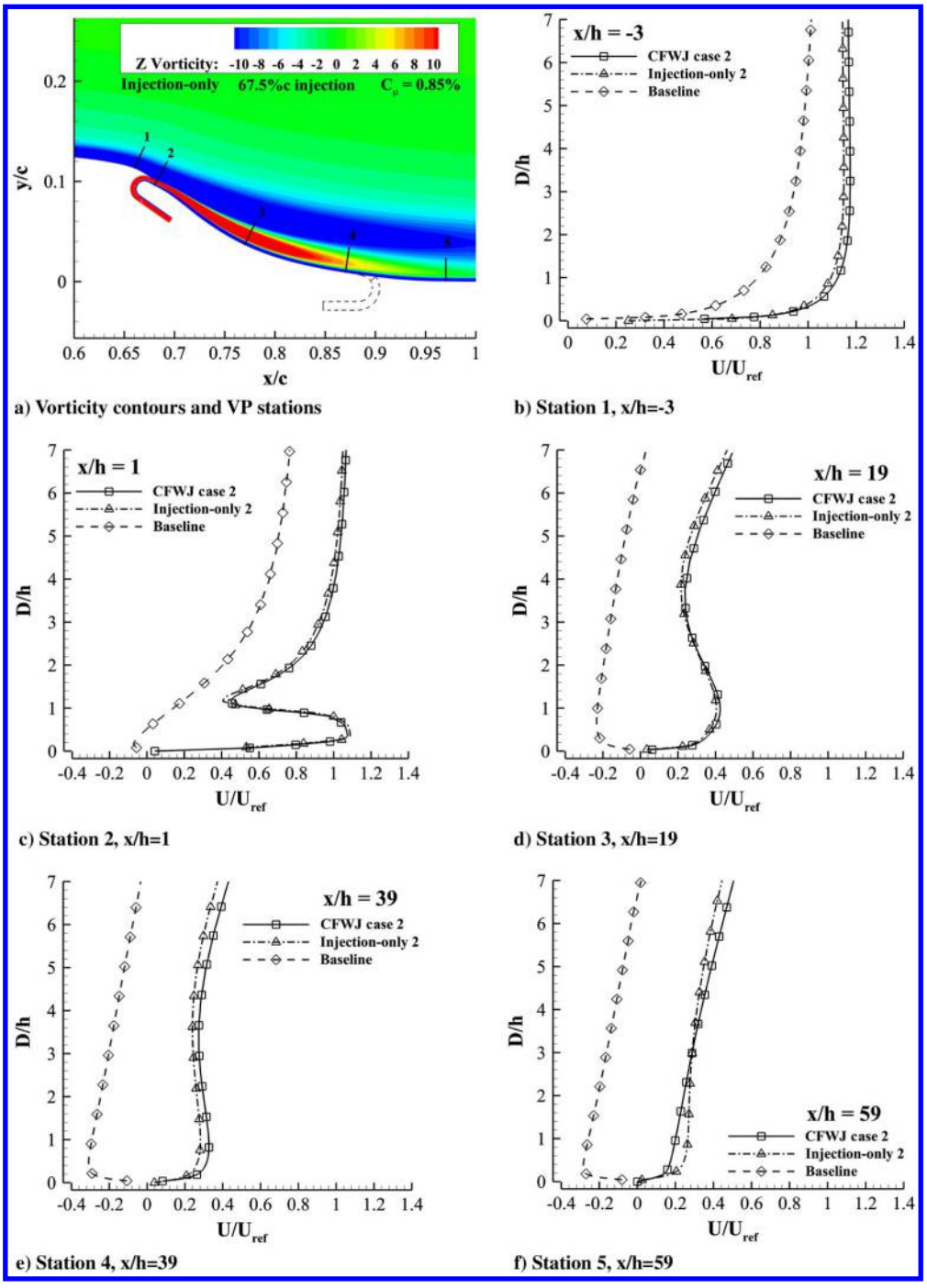

Fig. 24 The spanwise vorticity of the injection-only case 2 and the velocity profiles compared with the CFWJ case 2.

case 2 is slightly fuller than the CFWJ case 2 at the near-wall region. This appears to be caused by the blockage of the suction slot as shown by the zoomed plot in Fig. 25. The flow bifurcates around the suction slot lip and affects the flow near the wall. However, the overall flow is more energized as shown by the stronger outer flow in Fig. 24f.

Overall, the injection-only case 2 and CFWJ case 2 have very similar velocity profiles at all the streamwise stations. This is because the injection placed slightly downstream of the separation onset point plays a dominant role, which makes the suction not so important but more serves as the mass flow source for the injection. However, this does not mean that the injection-only flow control is as effective as the CFWJ in general. When the injection is placed away from the critical position slightly downstream of the separation onset point such as the injection-only case 1, CFWJ is more effective. In practical applications, the optimal position to place the injection is usually not known a priori.

These injection-only results give the following conclusions:

1) When the injection slot is far upstream of the separation onset point such as 50%c, the injection-only flow control is not as effective as the CFWJ case 9 that has a suction located at 70%c.

2) When the injection is located near the separation onset point as the CFWJ case 2, the injection-only flow control with the same C_μ appears as effective as the CFWJ case 2 in terms of flow attachment for this NASA hump configuration. However, even with the same control effectiveness, the CFWJ always has an advantage that it is ZNMF, which requires no external flow source.

The mentioned conclusions are consistent with the observation for the CFWJ cases 2 and 7 in Sec. IV.B.2, for which the suction location at 85 and 90%c yields the same CFWJ power coefficient because the CFWJ injection plays the dominant role to suppress the flow separation.

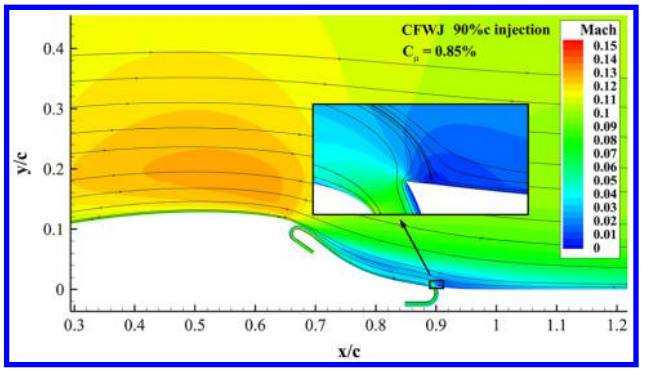

Fig. 25 Streamlines of CFWJ case 2 with zoomed view to show VP difference at stations 4 and 5.

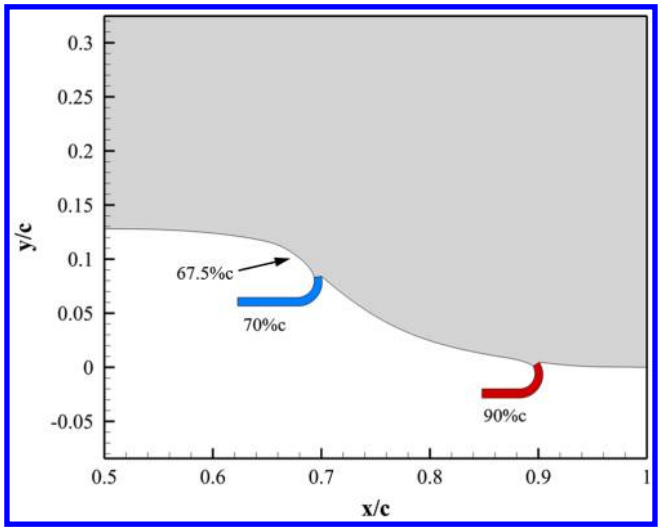

Fig. 26 Suction location trade study (suction-only cases 1, 2 and 3).

2. Suction-Only Flow Control

Following the same approach, for the suction-only study, the injection slots of the CFWJ cases 2 and 9 are removed, and the same suction slot located at 70 and 90%c (suction-only cases 2 and 3) are used. To increase the samples of the trade study, the suction location of the CFWJ case 8 is also adopted with the location at 67.5%c (suction-only case 1) as indicated by an arrow in Fig. 26, which shows the suction locations of the three suction-only cases 1, 2, and 3. For the CFWJ cases, the momentum coefficient C_μ is calculated based on the injection jet. For the suction-only trade study, the C_μ has to be calculated based on the suction. The C_μ of 0.77% of the CFWJ case 9 is thus recalculated based on its suction flow condition, and the corresponding C_μ is 0.57%.

Figure 27 shows the Mach number contours of the three suction-only cases with the suction slot at 67.5, 70, and 90%c. The minimum C_μ to make the flow attached is 0.61% for suction-only case 2 with the suction located at 70%c, 7% higher than 0.57% of the CFWJ case 9. The suction-only case 1 with the suction slot at 67.5%c has a very small separation zone. The suction-only Case 3 with the slot at 90%c (Fig. 27c), the same as that of the CFWJ case 2, has a large flow separation as shown in Fig. 27c with C_μ of 0.57%. The separation remains even with the C_μ increased by ten times.

The results of this suction-only study indicate that if the suction slot is placed at the optimal location downstream of the separation onset point at 70%c it is able to attach the flow, but the required C_μ is higher than that of the CFWJ optimum case 9. If the suction slot is off the optimal position, the CFWJ is much more effective becasue injection and suction all contribute to separation control.

Figure 28 shows the spanwise vorticity contours and the VPs of suction-only case 2 compared with the CFWJ case 9 (with its injection slot shown as the dash lines in Fig. 28a) and the baseline hump with no flow control. A significant difference of the vorticity contours from that of case 9 shown in Fig. 28b is that the suction-only case 2 has no counterrotating vorticity layers within the boundary layer. There is only one clockwise vorticity layer as a typical wall boundary layer. In other words, the suction-only flow control does not generate a wall jet as defined by Launder and Rodi [35].

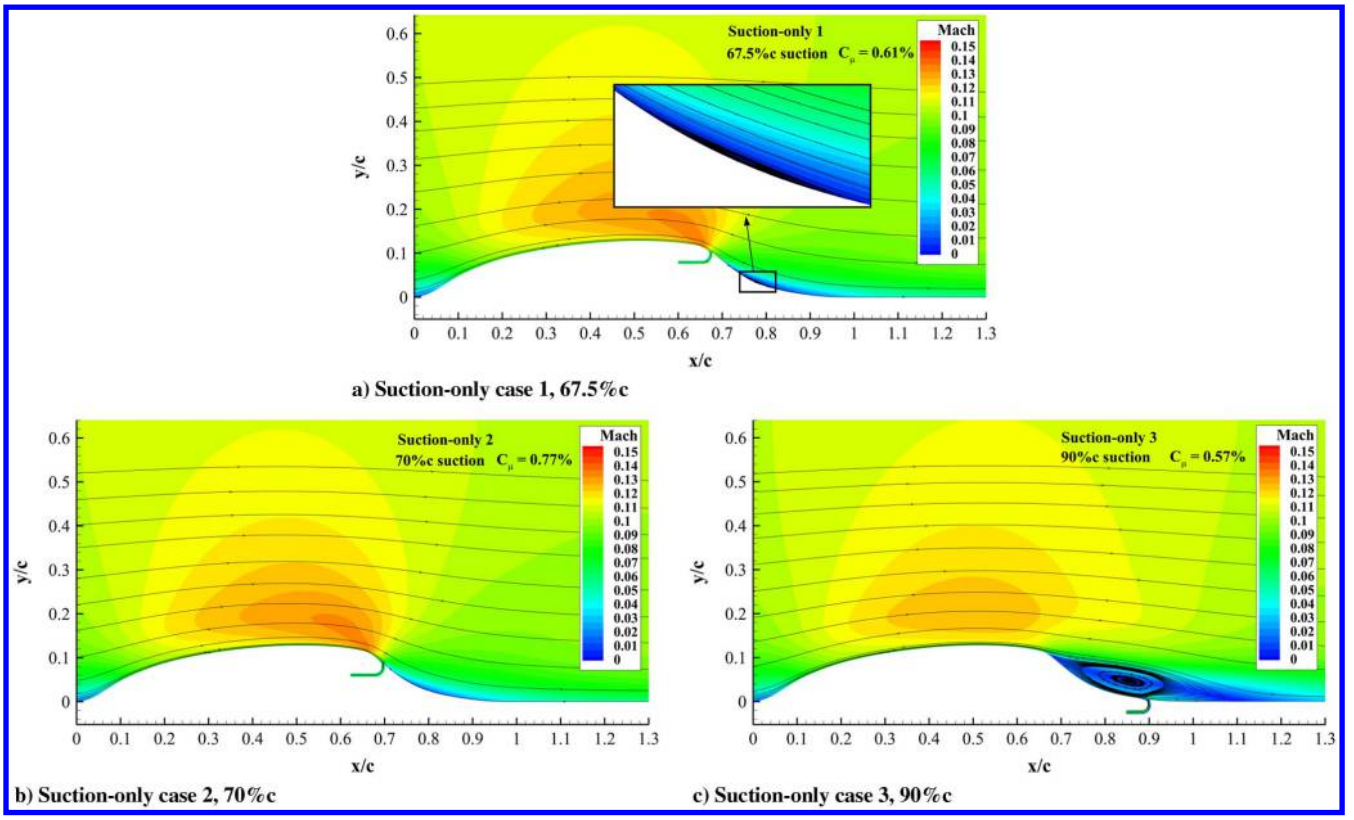

Fig. 27 Suction-only trade study.

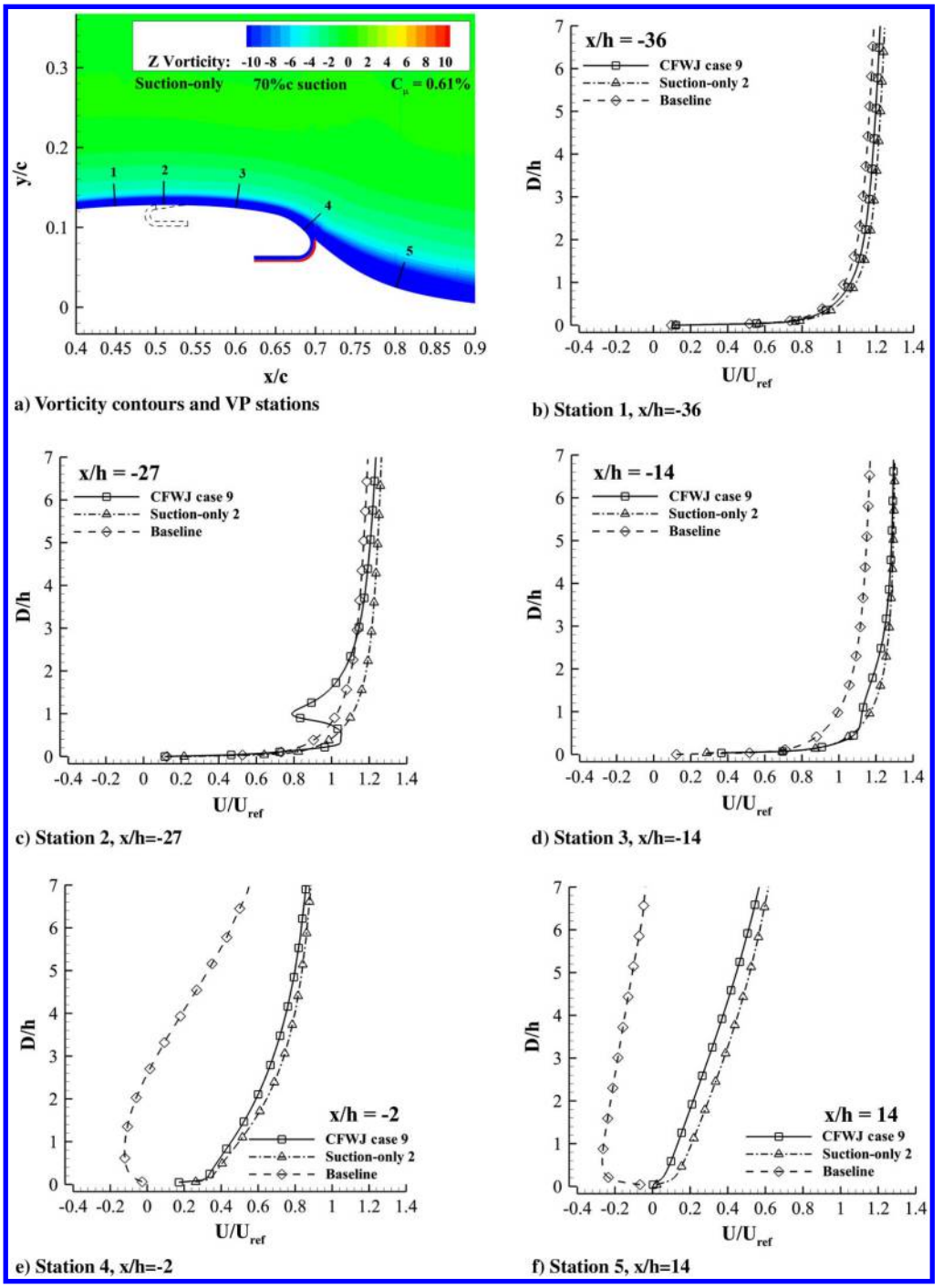

Fig. 28 The spanwise vorticity of the suction-only case 2 and the velocity profiles compared with the CFWJ case 9.

Figures 28b–28f compare the velocity profiles at five streamwise stations for the baseline NASA hump, the CFWJ case 9, and the suction-only case 2. The station locations are measured from the suction slot, and the distance is normalized by the suction slot height. As previously mentioned, the CFWJ case 9 has the same suction slot location as the suction-only case 2, but the C_μ of the CFWJ case 9 is 7% smaller. At station 1 located at 36 slot heights upstream of the suction slot, the VP of the suction-only flow control is the fullest among the three profiles, fuller than that of the CFWJ case 9 that has the injection located nearby downstream of station 1. This indicates that the low-pressure effects of the streamwise suction can propagate far upstream in the subsonic field. The VP of the baseline hump is the weakest. However, the overall difference of the three VPs is not large at this location far upstream of the separation region. At station 2, 27 slot-height upstream of the suction slot, the VP difference between the baseline and suction-only case is significantly increased. A wall jet shape VP is formed by the CFWJ case 9. At station 3, the wall jet counterclockwise vorticity layer of the CFWJ case 9 diminishes due to the favorable pressure gradient [77]. At station 4 immediately upstream of the suction slot, the VPs of the CFWJ and suction-only case are very similar without a wall jet protruding velocity profile shape. However, both the flow-controlled VPs are significantly energized compared with the separated VP of the baseline case. From stations 4 to 5, the flow decelerates in the adverse pressure gradient but remains attached for both the controlled flows, whereas the baseline hump is severely separated. The CFWJ case 9 has a C_μ of 7% smaller than that of the suction-only case, but it is the suction of the CFWJ case 9 that plays the dominant role to remove the flow separation because the injection-only case at the same upstream location does not remove the flow separation as shown in Fig. 23a.

By comparing the CFWJ cases with the injection-only case in Fig. 24 and the suction-only case in Fig. 28, it can be concluded that

for CFWJ injection or suction the one close to the separation onset plays the dominant role in suppressing flow separation. To maximize the CFWJ efficiency, there is a desirable distance between the injection and suction, which should be sufficiently long to allow a full mixing. For the injection or suction that is far away from the separation onset point, their effect on the separation suppressing is weak but primarily serves as the source or sink to satisfy the mass conservation and achieve ZNMF. Both the injection-only and suction-only flow controls are effective if the slots are placed at the optimal position slightly downstream of the separation onset point. If they are off their optimal location, the injection-only or suction-only flow controls are far less effective than the CFWJ.

V. Conclusions

The energy expenditure of coflow wall jet active flow control for the NASA hump is investigated numerically by trade studies of the injection and suction slot location. The injection-only and suction-only flow control methods are also studied and compared with the CFWJ. The following are some conclusions obtained from the validated numerical simulation using two-dimensional URANS with the Spalart–Allmaras turbulence model:

1) The power required of a CFWJ fluidic actuator is exponentially determined by the total pressure ratio and linearly determined by the mass flow rate. To minimize the coefficient of power required P_c, reducing the total pressure loss is more important than reducing the mass flow rate. This principle applies to general AFC using fluidic actuators. The momentum coefficient C_μ should not be used to measure AFC energy consumption because a low C_μ may yield a high power required due to a high total pressure ratio even though the mass flow rate is low. The quantitative value of C_μ is also very different from P_c.

2) The CFWJ is effective in both adverse and favorable pressure gradients but is more energy efficient to be used in adverse pressure gradients due to lower flow velocity, lower entropy increase, and enhanced mixing. As a result, the APG generates less main flow loss and thus requires a lower total pressure ratio of the CFWJ actuators.

3) To minimize the CFWJ energy expenditure, it is important to provide a sufficiently long distance between the injection and suction for thorough mixing and energy transfer in adverse pressure gradients. It is observed in this study that the distance with the counterclockwise vorticity layer vanishing is sufficient.

4) Both the tangential injection and streamwise suction of CFWJ are effective to suppress flow separation. It is most efficient to apply the injection or the suction near the flow separation onset point at a slightly downstream location in adverse pressure gradients. For this NASA hump, it is observed that the optimal suction location near the separation onset point is a little downstream of the optimal injection location.

5) Placing the injection of the CFWJ in the deep flow separation region is not able to remove the flow separation, but placing suction of CFWJ in the deep flow separation region is able to remove the flow separation attributed to the coupling effect of the upstream CFWJ injection.

6) For the injection-only or suction-only flow control, when the slots are at the optimal location downstream of the flow separation onset point, the injection-only flow control is as effective as the CFWJ for suppressing flow separation. The suction-only flow control needs a momentum coefficient 7% higher than that of the CFWJ to suppress the flow separation. However, if the slots are placed off the optimal position, the CFWJ flow control is much more effective and efficient than the injection-only or suction-only flow control.

Acknowledgments

The authors would like to acknowledge the computing resource provided by the Center of Computational Sciences at the University of Miami. The University of Miami and Gecheng Zha may receive royalties for future commercialization of the intellectual property used in this study. The University of Miami is also an equity owner in CoFlow Jet, LLC, licensee of the intellectual property used in this study.

References

[1] Gad-el-Hak, M., *Flow Control, Passive, Active, and Reactive Flow Management*, Cambridge Univ. Press, Cambridge, England, U.K., 2000.
https://doi.org/10.1017/CBO9780511529535

[2] Prandtl, L., and Teitjens, O. G., *Applied Hydro-and Aeromechanics*, Dover Books on Aeronautical Engineering, Vol. 2, Dover, New York, 1934.

[3] Glezer, A., and Amitay, M., "Synthetic Jets," *Annual Review of Fluid Mechanics*, Vol. 24, 2002.
https://doi.org/10.1146/annurev.fluid.34.090501.094913

[4] Jain, M., Puranik, B., and Agrawal, A., "A Numerical Investigation of Effects of Cavity and Orifice Parameters on the Characteristics of a Synthetic Jet Flow," *Sensors and Actuators A: Physical*, Vol. 165, No. 2, 2011, pp. 351–366.
https://doi.org/10.1016/j.sna.2010.11.001

[5] Mu, H., Yan, Q., Wei, W., and Sullivan, P.E., "Synthetic Jet Performance for Different Axisymmetric Cavities Analyzed with Three-Dimensional Lattice-Boltzmann Method," *AIAA Journal*, Vol. 56, No. 6, 2018, pp. 2499–2505.
https://doi.org/10.2514/1.J056921

[6] Kotapati, R. B., Mittal, R., and Cattafesta, L. N., III, "Numerical Study of a Transitional Synthetic Jet in Quiescent External Flow," *Journal of Fluid Mechanics*, Vol. 581, May 2007, pp. 287–321.
https://doi.org/10.1017/S0022112007005642

[7] Greenblatt, D., Paschal, K. B., Yao, C. S., and Harris, J., "Experimental Investigation of Separation Control Part 2: Zero Mass-Flux Oscillatory Blowing," *AIAA Journal*, Vol. 44, No. 12, 2006, pp. 2831–2845.
https://doi.org/10.2514/1.19324

[8] Tang, G., and Agarwal, R. K., "Numerical Simulation of Flow Control over NASA Hump with Uniform Blowing Jet and Synthetic Jet," *2018 Flow Control Conference*, AIAA Paper 2018-4017, 2018.
https://doi.org/10.2514/6.2018–4017

[9] Thomas, F., Kozlov, A., and Corke, T. C., "Plasama Actuators for Cylinder Flow Control and Noise Reduction," *AIAA Journal*, Vol. 46, May 2008, pp. 1921–1931.
https://doi.org/10.2514/1.27821

[10] Zhang, Z., Wu, Y., Jia, M., Song, H., Sun, Z., Zong, H., and Li, Y., "The Multichannel Discharge Plasma Synthetic Jet Actuator," *Sensors and Actuators A: Physical*, Vol. 253, Jan. 2017, pp. 112–117.
https://doi.org/1016/j.sna.2016.11.011

[11] Enloe, C. L., Mangina, R. S., and Font, G. I., "Normalized Electronegative Species Effects in the Dielectric-Barrier-Discharge Plasma Actuator," *AIAA Journal*, Vol. 54, No. 7, 2016, pp. 2061–2068.
https://doi.org/10.2514/1.J054551

[12] Shen, L., and Wen, C., "Leading Edge Vortex Control on a Delta Wing with Dielectric Barrier Discharge Plasma Actuators," *Applied Physics Letters*, Vol. 110, No. 25, 2017, Paper 251904.
https://doi.org/10.1063/1.4989901

[13] Sujar-Garrido, P., Benard, N., Moreau, E., and Bonnet, J. P., "Dielectric Barrier Discharge Plasma Actuator to Control Turbulent Flow Downstream of a Backward-Facing Step," *Experiments in Fluids*, Vol. 56, No. 4, 2015, p. 70.
https://doi.org/10.1007/s00348-015-1939-1

[14] Crowther, W., and Gomes, L., "An evaluation of the Mass and Power Scaling of Synthetic Jet Actuator Flow Control Technology for Civil Transport Aircraft Applications," *Proceedings of the Institution of Mechanical Engineers, Part I: Journal of Systems and Control Engineering*, Vol. 222, No. 5, 2008, pp. 357–372.
https://doi.org/10.1243/09596518 JSCE519

[15] Gil, P., and Strzelczyk, P., "Performance and Efficiency of Loudspeaker Driven Synthetic Jet Actuator," *Experimental Thermal and Fluid Science*, Vol. 76, Sept. 2016, pp. 163–174.
https://doi.org/10.1016/j.expthermflusci.2016.03.020

[16] Trávnček, Z., and Kordk, J., "Energetic Efficiencies of Synthetic Jet Actuators: Commentary on the Article by Gil and Strzelczyk," *Experimental Thermal and Fluid Science*, Vol. 98, Nov. 2018, pp. 121–123.
https://doi.org/10.1016/j.expthermflusci.2018.05.025

[17] Zito, J., Arnold, D., Houba, T., Soni, J., Durscher, R., and Roy, S., "Microscale Dielectric Barrier Discharge Plasma Actuators: Performance Characterization and Numerical Comparison," *43rd AIAA Plasmadynamics and Lasers Conference*, AIAA Paper 2012-3091, June 2012.
https://doi.org/10.2514/6.2012-3091

[18] Englar, R. J., and Williams, R. M., "Test Techniques for High Lift, Two Dimensional Airfoils with Boundary Layer and Circulation Control for Application to Rotary Wing Aircraft," *Canadian Aeronautics and Space Journal*, Vol. 19, July 1973, pp. 93–108.

[19] Englar, R. J., "Circulation Control for High Lift and Drag Generation on STOL Aircraft," *Journal of Aircraft*, Vol. 12, May 1975, pp. 457–463. https://doi.org/10.2514/3.59824

[20] Englar, R. J., "Circulation Control Pneumatic Aerodynamics: Blown Force and Moment Augmentation and Modifications; Past, Present and Future," AIAA Paper 2000-2541, June 2000. https://doi.org/10.2514/6.2000-2541

[21] Jones, G. S., "Pneumatic Flap Performance for a 2D Circulation Control Airfoil, Stedy & Pulsed," *Applications of Circulation Control Technologies*, edited by R. D. Joslin, and G. S. Jones, Vol. 214, Progress in Astronautics and Aeronautics, AIAA, Reston, VA, 2006, pp. 191–244, Chap. 7. https://doi.org/10.2514/4.866838

[22] Zha, G.-C., Paxton, C., Conley, A., Wells, A., and Carroll, B., "Effect of Injection Slot Size on High Performance Co-Flow Jet Airfoil," *Journal of Aircraft*, Vol. 43, 2006. https://doi.org/10.2514/1.16999

[23] Zha, G.-C., Carroll, B., Paxton, C., Conley, A., and Wells, A., "High Performance Airfoil Using Co-Flow Jet Flow Control," *AIAA Journal*, Vol. 45, Aug. 2007. https://doi.org/10.2514/1.20926

[24] Lefebvre, A., Dano, B., Bartow, W., Di Franzo, M., and Zha, G.-C., "Performance and Energy Expenditure of Co-Flow Jet Airfoil with Variation of Mach Number," *Journal of Aircraft*, Vol. 53, June 2016, pp. 1757–1767. https://doi.org/10.2514/1.C033113

[25] Yang, Y.-C., and Zha, G.-C., "Super-Lift Coefficient of Active Flow Control Airfoil: What Is the Limit?" *AIAA SCITECH2017, 55th AIAA Aerospace Science Meeting*, AIAA Paper 2017-1693, Jan. 2017. https://doi.org/10.2514/6.2017-1693

[26] Zha, G.-C., Yang, Y., Ren, Y., and McBreen, B., "Super-Lift and Thrusting Airfoil of Coflow Jet Actuated by Micro-Compressors," *2018 Flow Control Conference*, AIAA Paper 2017-3061, 2018. https://doi.org/10.2514/6.2018-3061

[27] Zha, G.-C., Gao, W., and Paxton, C. D., "Jet Effects on Co-Flow Jet Airfoil Performance," *AIAA Journal*, Vol. 45, June 2007, pp. 1222–1231. https://doi.org/10.2514/1.23995

[28] Wang, B.-Y., Haddoukessouni, B., Levy, J., and Zha, G.-C., "Numerical Investigations of Injection Slot Size Effect on the Performance of Co-Flow Jet Airfoil," *Journal of Aircraft*, Vol. 45, May 2008. https://doi.org/10.2514/1.37441

[29] Xu, K., and Zha, G.-C., "High Control Authority 3D Aircraft Control Surfaces Using Co-Flow Jet," *Journal of Aircraft*, Vol. 58, July 2020. https://doi.org/10.2514/1.C035727

[30] Forthmann, E., "Turbulent Jet Expansion," NACA TM-789, March 1936.

[31] Glauert, M. B., "The Wall Jet," *Journal of Fluid Mechanics*, Vol. 1, March 1956, pp. 625–643. https://doi.org/10.1017/S002211205600041X

[32] Bradshaw, P., and Gee, M. T., "Turbulent Wall Jets with and Without an External Stream," Aeronautical Research Council R&M 3252, 1960.

[33] Newman, B. G., "The Prediction of Turbulent Jets and Wall Jet," *Canadian Aeronautics and Space Journal*, Vol. 15, Jan. 1969.

[34] Irwin, H. P. A., "Measurement in a Self-Preserving Plane Wall Jet in a Positive Pressure Gradient," *Journal of Fluid Mechanics*, Vol. 61, March 1973, pp. 33–63. https://doi.org/10.1017/S0022112073000558

[35] Launder, B. E., and Rodi, W., "The Turbulent Wall Jet—Measurement and Modeling," *Journal of Fluid Mechanics*, Vol. 15, Jan. 1983, pp. 429–59. https://doi.org/10.1146/annurev.fl.15.010183.002241

[36] Neuendorf, R., and Wygnanski, I., "On a Turbulent Wall Jet Flowing over a Circular Cylinder," *Journal of Fluid Mechanics*, Vol. 381, Feb. 1999, pp. 1–25. https://doi.org/10.1017/S0022112098003668

[37] Xu, K., Ren, Y., and Zha, G.-C., "Numerical Investigation of NASA Hump Using Co-Flow Jet for Separation Control," *AIAA Scitech 2020 Forum*, AIAA Paper 2020-1058, 2020. https://doi.org/10.2514/6.2020-1058

[38] Xu, K., Ren, Y., and Zha, G.-C., "Separation Control by Co-Flow Wall Jet," *AIAA 2021 Aviation Forum*, AIAA Paper 2021-2946, June 2021. https://doi.org/10.2514/6.2021-2946

[39] Xu, K., and Zha, G.-C., "Mitigation of Serpentine Duct Flow Distortion Using Coflow Jet Active Flow Control," *AIAA Aviation 2020 Forum*, AIAA Paper 2020-2954, June 2020. https://doi.org/10.2514/6.2020-2954

[40] Xu, K., and Zha, G.-C., "Distortion Elimination for Serpentine Inlet Using CoFlow Jet Flow Control with Variation of Mach Numbers," *AIAA Propulsion and Energy 2020 Forum*, AIAA Paper 2020-3775, 2020. https://doi.org/10.2514/6.2020-3775

[41] Wang, Y., and Zha, G.-C., "Study of Super-Lift Coefficient of Co-Flow Jet Airfoil and Its Power Consumption," *AIAA Aviation 2019, AIAA Applied Aerodynamics Conference*, June 2019. https://doi.org/10.2514/6.2019-3652

[42] Barrios, P.A., Ren, Y., Xu, K., and Zha, G.-C., "Design of 3d Co-Flow Jet Airfoil with Integrated Micro-Compressor for High Operating Efficiency at Cruise Condition," *AIAA Aviation 2021*, AIAA Paper 2021-2581, June 2021. https://doi.org/10.2514/6.2021-2581

[43] Xu, K., and Zha, G.-C., "Design of High Specific Speed Mixed Flow Micro-Compressor for Co-Flow Jet Actuators," *IGTI Turbo Expo 2019*, American Soc. of Mechanical Engineers Paper GT2019-90980, Phoenix, AZ, June 2019. https://doi.org/10.1115/GT2019-90980

[44] Patel, P., and Zha, G.C., "Investigation of Mixed Micro-Compressor Casing Treatment Using Non-Matching Mesh Interface," *ASME Turbo Expo 2019 Turbomachinery Technical Conference and Exposition*, American Soc. of Mechanical Engineers Paper GT2019-90977, Phoenix, Arizona, 2019.

[45] Greenblatt, D., and Wygnanski, I. J., "The Control of Flow Separation by Periodic Excitation," *Progress in Aerospace Sciences*, Vol. 36, No. 7, 2000, pp. 487–545. https://doi.org/10.1016/S0376-0421(00)00008-7

[46] Wang, Y., and Zha, G.-C., "Study of 3D Co-Flow Jet Wing Induced Drag and Power Consumption at Cruise Conditions," *AIAA SciTech 2019*, AIAA Paper 2019-0034, Jan. 2019. https://doi.org/10.2514/6.2019-0034

[47] Wang, Y., and Zha, G.-C., "Study of Mach Number Effect for 2D Co-Flow Jet Airfoil at Cruise Conditions," *AIAA Aviation 2019, AIAA Applied Aerodynamics Conference*, AIAA Paper 2019-3169, June 2019.

[48] Zhang, J., Xu, K., Yang, Y., Ren, Y., Patel, P., and Zha, G.-C., "Aircraft Control Surfaces Using Co-flow Jet Active Flow Control Airfoil," *2018 Applied Aerodynamics Conference*, AIAA Paper 2018-3067, June 2018. https://doi.org/10.2514/6.2018-3067

[49] Xu, K., Zhang, J., and Zha, G.-C., "Drag Minimization of Co-Flow Jet Control Surfaces at Cruise Conditions," *AIAA Scitech 2019 Forum*, AIAA Paper 2019-1848, Jan. 2019. https://doi.org/10.2514/6.2019-1848

[50] Greenblatt, D., Paschal, K. B., Yao, C. S., Harris, J., Schaeffler, N. W., and Washburn, A. E., "Experimental Investigation of Separation Control Part 1: Baseline and Steady Suction," *AIAA Journal*, Vol. 44, No. 12, 2006, pp. 2820–2830. https://doi.org/10.2514/1.13817

[51] Rumsey, C., "2DWMH: 2D NASA Wall-Mounted Hump Separated Flow Validation Case," *Turbulence Modeling Resource*, NASA Langley Research Center, 2003, https://turbmodels.larc.nasa.gov/nasahump_val.html [retrieved 18 Nov. 2021].

[52] Seifert, A., and Pack, L. G., "Active Flow Separation Control on Wall-Mounted Hump at High Reynolds Numbers," *AIAA Journal*, Vol. 40, No. 7, 2002, pp. 1363–1372. https://doi.org/10.2514/2.1796

[53] Koklu, M., "A Numerical and Experimental Investigation of Flow Separation Control over a Wall-Mounted Hump Model," *2018 AIAA Aerospace Sciences Meeting*, AIAA Paper 2018-1280, 2018. https://doi.org/10.2514/6.2018-1280

[54] Borgmann, D., Pande, A., Little, J., and Woszidlo, R., "Experimental Study of Discrete Jet Forcing for Flow Separation Control on a Wall Mounted Hump," *AIAA SciTech 2017, 55th AIAA Aerospace Sciences Meeting*, AIAA Paper 2017-1450, Jan. 2017. https://doi.org/10.2514/6.2017-1450

[55] Koklu, M., "Steady and Unsteady Excitation of Separated Flow over the NASA Hump Model," *2018 Flow Control Conference*, AIAA Paper 2018-4016, 2018. https://doi.org/10.2514/6.2018-4016

[56] Kara, K., Kim, D., and Morris, P. J., "Flow-Separation Control Using Sweeping Jet Actuator," *AIAA Journal*, Vol. 56, No. 11, 2018, pp. 4604–4613. https://doi.org/10.2514/1.J056715

[57] Koklu, M., "Application of Sweeping Jet Actuators on the NASA Hump Model and Comparison with CFDVAL2004 Experiments," *47th AIAA*

Fluid Dynamics Conference, AIAA Paper 2017-3313, 2017.
https://doi.org/10.2514/6.2017-3313

[58] Spalart, P. R., and Allmaras, S. R., "A One-Equation Turbulence Model for Aerodynamic Flows," *30th Aerospace Sciences Meeting and Exhibit*, AIAA Paper 1992-0439, Jan. 1992.
https://doi.org/10.2514/6.1992-439

[59] Zha, G.-C., and Bilgen, E., "Numerical Study of Three-Dimensional Flows Using Unfactored Upwind-Relaxation Sweeping Algorithm," *Journal of Computational Physics*, Vol. 125, No. 2, 1996, pp. 425–433.
https://doi.org/10.1006/jcph.1996.0104

[60] Shen, Y.-Q., and Zha, G.-C., "Improved Seventh-Order WENO Scheme," *48th AIAA Aerospace Sciences Meeting*, AIAA Paper 2010-1451, Jan. 2010.
https://doi.org/10.2514/6.2010-1451

[61] Zha, G.-C., Shen, Y.-Q., and Wang, B., "An Improved Low Diffusion E-CUSP Upwind Scheme," *Computer & Fluids*, Vol. 48, Sept. 2011, pp. 214–220.
https://doi.org/10.1016/j.compfluid.2011.03.012

[62] Shen, Y.-Q., Zha, G.-C., and Wang, B.-Y., "Improvement of Stability and Accuracy for Weighted Essentially Nonoscillatory Scheme," *AIAA Journal*, Vol. 47, May 2009, pp. 331–344.
https://doi.org/10.2514/1.37697

[63] Shen, Y.-Q., Zha, G.-C., and Chen, X.-Y., "High Order Conservative Differencing for Viscous Terms and the Application to Vortex-Induced Vibration Flows," *Journal of Computational Physics*, Vol. 228, No. 2, 2009, pp. 8283–8300.
https://doi.org/10.1016/j.jcp.2009.08.004

[64] Shen, Y.-Q., and Zha, G.-C., "Improvement of the WENO Scheme Smoothness Estimator," *International Journal for Numerical Methods in Fluids*, Vol. 64, Sept. 2010.
https://doi.org/10.1002/fld.2186

[65] Zha, G.-C., and Bilgen, E., "Numerical Solutions of Euler Equations by Using a New Flux Vector Splitting Scheme," *International Journal for Numerical Methods in Fluids*, Vol. 17, July 1993, pp. 115–144.
https://doi.org/10.1002/fld.1650170203

[66] Chen, X., and Zha, G.-C., "Fully Coupled Fluid–Structural Interactions Using an Efficient High Resolution Upwind Scheme," *Journal of Fluids and Structures*, Vol. 20, No. 8, 2005, pp. 1105–1125.
https://doi.org/10.1016/j.jfluidstructs.2005.02.011

[67] Wang, B.-Y., and Zha, G.-C., "A General Sub-Domain Boundary Mapping Procedure For Structured Grid CFD Parallel Computation," *Journal of Aerospace Computing, Information, and Communication*, Vol. 5, No. 11, 2008, pp. 2084–2091.
https://doi.org/10.2514/1.35498

[68] Dano, B. P. E., Kirk, D., and Zha, G.-C., "Experimental Investigation of Jet Mixing Mechanism of Co-Flow Jet Airfoil," *5th AIAA Flow Control Conference*, AIAA Paper 2010-4421, June–July 2010.
https://doi.org/10.2514/6.2010-4421

[69] Dano, B. P. E., Zha, G.-C., and Castillo, M., "Experimental Study of Co-Flow Jet Airfoil Performance Enhancement Using Micro Discreet Jets," *49th AIAA Aerospace Sciences Meeting*, AIAA Paper 2011-0941, Jan. 2011.
https://doi.org/10.2514/6.2011-941

[70] Lefebvre, A., and Zha, G.-C., "Design of High Wing Loading Compact Electric Airplane Utilizing Co-Flow Jet Flow Control," *AIAA SciTech2015: 53nd Aerospace Sciences Meeting*, AIAA Paper 2015-0772, Jan. 2015.
https://doi.org/10.2514/6.2015-0772

[71] Liu, Z.-X., and Zha, G.-C., "Transonic Airfoil Performance Enhancement Using Co-Flow Jet Active Flow Control," *AIAA Aviation*, AIAA Paper 2016-3066, June 2016.
https://doi.org/10.2514/6.2016-3472

[72] Lefebvre, A., and Zha, G.-C., "Trade Study of 3D Co-Flow Jet Wing for Cruise Performance," *AIAA SCITECH2016, AIAA Aerospace Science Meeting*, AIAA Paper 2016-0570, Jan. 2016.
https://doi.org/10.2514/6.2016-0570

[73] Naughton, J. W., Viken, S., and Greenblatt, D., "Skin Friction Measurements on the NASA Hump Model," *AIAA Journal*, Vol. 44, No. 6, 2006, pp. 1255–1265.
https://doi.org/10.2514/1.14192.

[74] McGahan, W. A., "The Incompressible, Turbulent Wall Jet in an Adverse Pressure Gradient," Massachusetts Inst. of Technology Rept. 82, Cambridge, MA, 1965.

[75] Uzun, A., and Malik, M. R., "Wall-Resolved Large-Eddy Simulation of Flow Separation over NASA Wall-Mounted Hump," *55th AIAA Aerospace Sciences Meeting*, AIAA Paper 2017-0538, 2017.
https://doi.org/10.2514/6.2017-0538

[76] Denton, J. D., "Loss Mechanisms in Turbomachines," *ASME 1993 International Gas Turbine and Aeroengine Congress and Exposition*, American Soc. of Mechanical Engineers, Cincinnati, OH, 1993, pp. V002T14A001–V002T14A001.

[77] Greitzer, E. M., Tan, C. S., and Graf, M. B., *Internal Flow: Concepts and Applications*, Cambridge Univ. Press, Cambridge, England, U.K., 2004.
https://doi.org/10.1017/CBO9780511616709

J. Poggie
Associate Editor